A Stability Analysis and Some Numerical Computations for Thermal Convection with a Variable Buoyancy Factor

Fei Dong,[1] Albert T. Hsui,[2] and Daniel N.Riahi[1]

[1]Department of Theoretical and Applied Mechanics
[2]Department of Geology
University of Illinois at Urbana-Champaign
Urbana, IL 61801

Abstract: Linear and nonlinear analyses of thermal convection with a variable "buoyancy factor", which is defined as the product of thermal expansion coefficient and gravitational acceleration, are investigated for a fluid layer between two infinite horizontal plates. An isothermal boundary condition is applied for both boundaries, and the buoyancy factor throughout the fluid layer is chosen to be a function of depth. For various profiles of variable buoyancy factor, the associated eigenvalue problem for the linear regime is solved numerically using a spectral method. It is found that for the case of buoyancy factor deficit, where the vertical rate of change of the buoyancy factor is negative, the convective flow yields a higher critical Rayleigh number than that of the constant buoyancy factor case. For the case of buoyancy factor gain, where the vertical rate of change of the buoyancy factor is positive, the results are reversed. A formula for the critical Rayleigh number as a function of the statistical features of the buoyancy factor is developed. For the nonlinear regime, computations based on a spectral Fourier–Chebyshev collocation method are carried out for six parabolic profiles of buoyancy factor. Flow patterns are found to be dominated by two–dimensional rolls for the Rayleigh numbers considered. The computed Nusselt numbers indicate that buoyancy factor deficit (gain) yields lower (higher) heat flux when compared with the corresponding constant buoyancy factor case. When the buoyancy factor deficit is sufficiently large to produce sign changes in the profile, our numerical simulations show that multiple layering in the vertical direction can be produced.

Keywords: thermal convection, buoyancy factor, convective flow, buoyancy driven flow, natural convection.

1 Introduction

It is well known that thermal buoyancy is the driving factor for thermal convection. Both thermal expansion coefficient and gravity are involved in producing thermal buoyancy effects. In most thermal convection formulations, the product of thermal expansion coefficient and gravity represents the coefficient of thermal buoyancy. In this paper, therefore, we define this product as the "buoyancy factor".

Solid–state thermal convection has been used to model thermal histories of the interior of planets for many decades (see Schubert, 1995 for a recent review). For Cartesian modeling, the gravitational field was typically assumed to be constant throughout the convective domain. For spherical modeling, the gravity was taken to follow a linear function of radius, which represents the gravity within a homogeneous sphere. However, the gravitational field within a solid planet may not follow such a simple relationship, especially when a dense central core is present (Chandrasekhar, 1961). Consider the Earth as an example. Many investigators have studied the gravitational acceleration within the Earth's interior (Anderson and Hart, 1976; Stacey, 1992, for example). Gravitational acceleration at any point within the Earth's mantle is determined by its distance to the core and the amount of mantle materials underneath. It can be shown easily that mass associated with a spherically symmetric shell does not contribute to the gravitational acceleration at any interior point. Generally, the added mantle mass will increase the acceleration, whereas moving away from the core will decrease the acceleration. These two competing effects can produce rather peculiar gravitational acceleration profiles within the Earth's mantle. In fact, according to Stacey (1992), the gravitational acceleration within the Earth's core increases linearly with radius, which is consistent with that of a nearly uniform spherical body. Within the mantle, however, gravitational acceleration no longer follows the same trend. Instead, it shows a local minimum and a local maximum before it reaches the surface value of 9.8 m/sec^2. Deviation of the field can be as large as 8% from the surface value, but the effects of such an unusual gravitational field upon solid–state thermal convection have received very little attention. Therefore, it is the purpose of this paper to examine the dynamic behavior of thermal convection with a variable buoyancy factor, which includes cases with a variable gravitational field.

We know that the gravity is positive everywhere, and for most of the substances in nature, the thermal expansion coefficient is also positive, so the buoyancy factor usually keeps a positive sign throughout the flow field. However, some materials can show negative thermal expansion characteristics under specific temperature ranges. For example, ice has a maximum density at 4°C, which means that ice possesses negative thermal expansion coefficients below 4°C. Thus, for icy mantle convection within Europa, for example, a buoyancy factor inversion could exist. Meanwhile, Hsui and Riahi (2000)

pointed out that for thermal convection between nearly insulating and rigid boundaries, if the buoyancy factor changes sign within a convective domain, eigenfunctions of the stability analysis suggest that a multiple–layer flow structure may be possible. Therefore, it is also of interest to investigate the effects of buoyancy factor profiles that change signs within the flow field, and determine the corresponding dynamic behavior.

In this paper, we first present the mathematical formulation and the governing system for the perturbed dependent variables from a static basic state. A numerical solution for the linear stability of the basic state is then presented. Thereafter, fully nonlinear numerical simulations of the convective system are described and discussed, followed by conclusions and remarks.

2 Mathematical Formulation

2.1 Governing Equations

In this study, we choose to follow a Cartesian model for analytic simplicity. This study represents a first–order examination of the effects of nonuniform buoyancy factors on thermal convection.

Consider a fluid layer bounded by two infinite horizontal flat planes. In this model, the buoyancy factor within the layer is assumed to be a function of depth only. For completeness, a uniform heat source throughout the layer is included. In this model, the top boundary is assumed to be isothermal, whereas the bottom boundary can be either isothermal or insulating.

We start with the basic governing equations for a compressible flow in tensor notation. They are:

$$\frac{\partial \rho}{\partial t} + \frac{\partial}{\partial x_i}\left(\rho u_i\right) = 0\,, \tag{1}$$

$$\rho \frac{Du_i}{Dt} = -\frac{\partial p}{\partial x_i} + \frac{\partial \tau_{ki}}{\partial x_k} - \rho g \delta_{i3}\,, \tag{2}$$

$$\rho C_p \frac{DT}{Dt} - \alpha T \frac{Dp}{Dt} = \tau_{ik}\frac{\partial u_i}{\partial x_k} + \frac{\partial}{\partial x_i}\left(k\frac{\partial T}{\partial x_i}\right) + \rho H_0\,, \tag{3}$$

where

$$\left.\begin{aligned} \frac{D}{Dt} &\equiv \frac{\partial}{\partial t} + u_j \frac{\partial}{\partial x_j}\,, \\ \tau_{ik} &= \mu\left(\frac{\partial u_i}{\partial x_k} + \frac{\partial u_k}{\partial x_i}\right) + \xi \delta_{ik}\frac{\partial u_j}{\partial x_j}\,, \end{aligned}\right\} \tag{4}$$

The subscripts i, j, and k are the dummy space indices, and subscript "3" represents the vertical direction, which coincides with that of the gravity, μ is the viscosity, ρ is the density, $\vec{\mathbf{u}}=(u_1, u_2, u_3)$ is the velocity vector, $\vec{\mathbf{r}}=(x_1, x_2, x_3)$ is the position vector, g

is the gravity function, p is the pressure, T is the temperature, C_p is the specific heat at constant pressure, ρH_0 is the internal heat source per unit volume, δ_{i3} is the Kronecker delta, and ξ is the bulk viscosity, which is assumed to be $\left(-\frac{2}{3}\mu\right)$ according to the Stokes' hypothesis (White, 1991). The non–subscript k is the thermal conductivity. Both k and μ are taken to be constant.

2.2 Base State

For the base flow, we consider a steady, motionless field with constant density. Furthermore, pressure and temperature of the base flow are assumed to be functions of depth (x_3, or z) only. It follows that equations (1)−(3) for the base flow yield

$$p_0(z) = -\rho_0 \int_0^z g(z)\,\mathrm{d}z\,, \tag{5}$$

and

$$k\frac{\mathrm{d}^2 T_0}{\mathrm{d}z^2} = -\rho_0 H_0\,, \tag{6}$$

where the subscript "0" represents the base flow quantities.

Two different bottom thermal boundary conditions are considered here. In the first case, both boundaries are assumed to be isothermal, namely,

$$T_0(0) = \theta_\mathrm{B}\,, \quad T_0(h) = \theta_\mathrm{T}\,, \tag{7}$$

where subscripts "B" and "T" indicate the bottom and the top of the fluid layer, respectively, and h is the thickness of the fluid layer. The corresponding thermal profile for the base state is

$$T_0(z) = \theta_\mathrm{B} - \beta z + \frac{H_0}{2\kappa C_p} z(h-z)\,, \tag{8}$$

where $\beta \equiv \dfrac{\theta_\mathrm{B} - \theta_\mathrm{T}}{h}$ represents the negative of the basic temperature gradient across the fluid layer, and $\kappa \equiv \dfrac{k}{\rho_0 C_p}$ is the thermal diffusivity. In the second case, the bottom boundary is assumed to be insulating whereas the top is maintained as isothermal. Thus,

$$\frac{\mathrm{d}T_0}{\mathrm{d}z}(0) = 0\,, \quad T_0(h) = \theta_\mathrm{T}\,. \tag{9}$$

The thermal profile for the base state, in this case, becomes

$$T_0(z) = \theta_T + \frac{H_0}{2\kappa C_p}(h^2 - z^2) \tag{10}$$

We note that in the first case, because of the existence of an internal heat source, the energy input from the bottom boundary Q_{in}, as defined below, is not always positive even when $\theta_{\rm B} > \theta_{\rm T}$. In fact,

$$Q_{\rm in} = -k\frac{{\rm d}T_0}{{\rm d}z}(0) \begin{cases} > 0 & \text{if } \theta_{\rm B} - \theta_{\rm T} > \dfrac{H_0 h^2}{2\kappa C_p} \\ = 0 & \text{if } \theta_{\rm B} - \theta_{\rm T} = \dfrac{H_0 h^2}{2\kappa C_p} \\ < 0 & \text{if } \theta_{\rm B} - \theta_{\rm T} < \dfrac{H_0 h^2}{2\kappa C_p} \end{cases}$$

One can expect that the flow has different features corresponding to different signs for $Q_{\rm in}$. In other words, one can anticipate that the nondimensional parameter $H = \dfrac{H_0 h^2}{\kappa C_p(\theta_{\rm B} - \theta_{\rm T})}$ plays different roles depending on whether its value is smaller or larger than 2.

2.3 The Perturbed Governing Equations

To examine the deviation of the flow from the base state, the following disturbances are introduced:

$$\left.\begin{aligned} u_i &= u_i'(x,y,z,t) \quad (i = 1,2,3)\,, \\ p &= p_0(z) + p'(x,y,z,t)\,, \\ T &= T_0(z) + \theta'(x,y,z,t)\,, \\ \rho &= \rho_0(1 - \alpha\theta' + \chi p')\,, \end{aligned}\right\} \tag{11}$$

where the primed quantities ($u_i'\,, p'$, and θ') represent the dependent variables for the flow deviation from the base state derived in Section 2.2, α is the thermal expansion coefficient, and χ is the compressiblity coefficient. Substituting (11) into the governing equations (1)−(3), we have the following equations:

$$-\alpha\frac{\partial\theta'}{\partial t} + \chi\frac{\partial p'}{\partial t} + \frac{\partial u_i'}{\partial x_i} = 0\,, \tag{12}$$

$$\rho_0\left(\frac{\partial u_i'}{\partial t} + u_k'\frac{\partial u_i'}{\partial x_k}\right) = -\frac{\partial p'}{\partial x_i} + \frac{\partial \tau_{ki}'}{\partial x_k} - \rho_0 g\delta_{i3}(-\alpha\theta' + \chi p')\,, \tag{13}$$

$$\begin{aligned} &\rho_0 C_p\left(\frac{\partial\theta'}{\partial t} + u_k'\frac{\partial\theta'}{\partial x_k} + u_3'\frac{{\rm d}T_0}{{\rm d}z}\right) - \alpha T_0\left(u_3'\frac{{\rm d}p_0}{{\rm d}z} + \frac{\partial p'}{\partial t}\right) \\ &\qquad = k\frac{\partial^2\theta'}{\partial x_i \partial x_i} + \rho_0 H_0(-\alpha\theta' + \chi p')\,, \end{aligned} \tag{14}$$

where $\tau'_{ki} = \mu\left(\dfrac{\partial u'_i}{\partial x_k} + \dfrac{\partial u'_k}{\partial x_i} - \dfrac{2}{3}\delta_{ik}\dfrac{\partial u'_j}{\partial x_j}\right)$ is the perturbed viscous stress tensor.

For a nondimensionalization of the governing equations, the following characteristic scales are introduced:

$$\left.\begin{array}{lll} \text{Length: } h & \text{Velocity: } \dfrac{\kappa}{h} & \text{Time: } \dfrac{h^2}{\kappa} \\ \text{Density: } \rho_0 & \text{Pressure: } \dfrac{\kappa\mu}{h^2} & \text{Temperature: } T^* \\ \text{Gravity: } g_0 & \text{Heating: } \dfrac{\kappa C_p T^*}{h^2} & \text{Expansivity: } \alpha_0 \end{array}\right\} \tag{15}$$

Here h is the depth of the layer, g_0 is a characteristic gravitational acceleration, T^* is a characteristic temperature, and α_0 is a characteristic thermal expansion coefficient. For this study, we set g_0 and α_0 to be the corresponding values at the top boundary, and the choice of T^* varies with respect to the choice of the thermal boundary condition at the bottom. The following nondimensional parameters can then be introduced:

$$\left.\begin{array}{lll} \mathrm{Ra} = \dfrac{\alpha_0\rho_0 g_0 T^* h^3}{\mu\kappa}\,, & \mathrm{Pr} = \dfrac{\mu}{\rho_0\kappa}\,, & \mathrm{Di} = \dfrac{\alpha_0 g_0 h}{C_p} \\ \delta = \alpha_0 T^*\,, & K = \dfrac{\chi\mu\kappa}{\alpha_0 T^* h^2}\,, & H = \dfrac{H_0 h^2}{\kappa C_p T^*} \end{array}\right\} \tag{16}$$

For the Earth's mantle the nondimensional parameter δ is only a few percent (Jarvis and McKenzie, 1980) and K lies between 10^{-5} and 10^{-6} (Turcotte *et al.*, 1973). Therefore, it is reasonable to introduce the anelastic liquid assumption, which sets $\delta = K = 0$. We further assume that the viscous dissipation can be neglected, i.e. $\mathrm{Di} = 0$. Therefore, the important nondimensional parameters in this study become the Rayleigh number Ra, the Prandtl number Pr, and the internal heating parameter H. The resulting nondimensional equations for the disturbances are

$$\frac{\partial u_i}{\partial x_i} = 0\,, \tag{17}$$

$$\frac{1}{\mathrm{Pr}}\left(\frac{\partial u_i}{\partial t} + u_k\frac{\partial u_i}{\partial x_k}\right) = -\frac{\partial p}{\partial x_i} + \frac{\partial^2 u_i}{\partial x_k \partial x_k} + \mathrm{Ra}\alpha g\theta\delta_{i3}\,, \tag{18}$$

$$\frac{\partial\theta}{\partial t} + u_k\frac{\partial\theta}{\partial x_k} + f(z)u_3 = \frac{\partial^2\theta}{\partial x_i\partial x_i}\,, \tag{19}$$

where the primes have been dropped for notation simplicity, and $f(z)$ representing the nondimensional temperature gradient for the base state is given by

$$f(z) = \begin{cases} -\dfrac{\theta_\mathrm{B} - \theta_\mathrm{T}}{T^*} + \dfrac{H}{2}(1-2z) & \text{for case 1} \\ -Hz & \text{for case 2} \end{cases} \tag{20}$$

It is clear that the thermal expansion coefficient α and the gravity g appear only in pairs with each other in this model. Therefore we define the "buoyancy factor" $B \equiv \alpha g$ and hereafter discuss the effects of B only, rather than discussing the effects of α and g separately.

Regarding the choice of T^*, it is natural and customary to choose the temperature difference between the two boundaries as the characteristic temperature scale when the bounding temperatures are prescribed. For case 1, therefore, $T^* = \theta_{\rm B} - \theta_{\rm T}$ and $f(z) = -1 + \dfrac{H}{2}(1-2z)$. For case 2, a natural choice is $T^* = \dfrac{H_0 h^2}{\kappa C_p}$, which leads to $H = 1$ and $f(z) = -z$.

As to the boundary conditions for equations (17)−(19), three categories of boundary condition need to be considered: horizontal velocity conditions, vertical velocity conditions, and thermal conditions. For the horizontal velocity components, there are two possible choices for the boundary conditions: rigid ("no–slip") or stress–free. For a rigid boundary (denoted as "R" hereafter),

$$u_1 = u_2 = 0\,. \tag{21a}$$

For a stress–free boundary (denoted as "S" hereafter),

$$\frac{\partial u_1}{\partial z} = \frac{\partial u_2}{\partial z} = 0\,. \tag{21b}$$

Since the top and the bottom boundaries can possess different mechanical properties, a total of four combinations of boundary conditions need to be considered: RR, RS, SR, and SS, where the first letter stands for the boundary type at the bottom ($z = 0$), and the second letter stands for the boundary type at the top ($z = 1$). For the vertical velocity component, the most natural choice is the no–penetration condition, i.e.

$$u_3(x, y, 0, t) = u_3(x, y, 1, t) = 0\,. \tag{22}$$

Finally, for thermal boundary conditions, we have

$$\theta(x, y, 0, t) = \theta(x, y, 1, t) = 0 \tag{23a}$$

for case 1 and

$$\frac{\partial \theta}{\partial z}(x, y, 0, t) = 0, \quad \theta(x, y, 1, t) = 0 \tag{23b}$$

for case 2.

3 Stability Analysis and Numerical Method

In this section, we will consider stability of the basic motionless state, which was described in Section 2.2. The disturbances are assumed to be infinitesimal in

amplitude. As a result, the governing equations are described by (17)−(19) with the nonlinear terms dropped because they represent second–order terms.

3.1 Normal Mode Analysis

We assume that the nondimensional disturbances have the form

$$\left.\begin{aligned} u_i(x,y,z,t) &= \tilde{u}_i(z)\,\exp[\underline{i}(\sigma x+\gamma y-\omega t)] \quad (i=1,2,3)\,, \\ p(x,y,z,t) &= \tilde{p}(z)\,\exp[\underline{i}(\sigma x+\gamma y-\omega t)]\,, \\ \theta(x,y,z,t) &= \tilde{\theta}(z)\,\exp[\underline{i}(\sigma x+\gamma y-\omega t)]\,, \end{aligned}\right\} \tag{24}$$

where $\underline{i}\equiv\sqrt{-1}$ is the pure imaginary number, σ and γ are the wavenumbers in the x and y direction, respectively, and ω is the temporal growth rate of the disturbance. Furthermore, since x and y are interchangable in the linearized equations (17)−(19) and boundary conditions (21)−(23), we can, without loss of generality, consider two–dimensional disturbances only. In other words, we can set

$$u_2=0, \quad \gamma=0\,.$$

Using a two–dimensional version of (24) in the linearized form of the equations (17)−(19), we are led to the following equations:

$$\underline{i}\sigma\tilde{u}_1+\frac{\mathrm{d}\tilde{u}_3}{\mathrm{d}z}=0\,, \tag{25}$$

$$-\underline{i}\omega\tilde{u}_1=-\underline{i}\sigma\mathrm{Pr}\tilde{p}+\mathrm{Pr}\left(\frac{\mathrm{d}^2}{\mathrm{d}z^2}-\sigma^2\right)\tilde{u}_1\,, \tag{26}$$

$$-\underline{i}\omega\tilde{u}_3=-\mathrm{Pr}\frac{\mathrm{d}\tilde{p}}{\mathrm{d}z}+\mathrm{Pr}\left(\frac{\mathrm{d}^2}{\mathrm{d}z^2}-\sigma^2\right)\tilde{u}_3+\mathrm{RaPr}B\tilde{\theta}\,, \tag{27}$$

$$-\underline{i}\omega\tilde{\theta}=-f(z)\tilde{u}_3+\left(\frac{\mathrm{d}^2}{\mathrm{d}z^2}-\sigma^2\right)\tilde{\theta}\,. \tag{28}$$

Applying the two–dimensional forms of (24) in the boundary conditions (21)−(23), we find

$$\left\{\begin{aligned} &(\mathrm{RR}): \quad \tilde{u}_1(0)=\tilde{u}_1(1)=0\,, \\ &(\mathrm{RS}): \quad \tilde{u}_1(0)=0,\ \frac{\mathrm{d}\tilde{u}_1}{\mathrm{d}z}(1)=0\,, \\ &(\mathrm{SR}): \quad \frac{\mathrm{d}\tilde{u}_1}{\mathrm{d}z}(0)=0,\ \tilde{u}_1(1)=0\,, \\ &(\mathrm{SS}): \quad \frac{\mathrm{d}\tilde{u}_1}{\mathrm{d}z}(0)=\frac{\mathrm{d}\tilde{u}_1}{\mathrm{d}z}(1)=0\,, \end{aligned}\right. \tag{29}$$

$$\tilde{u}_3(0)=\tilde{u}_3(1)=0\,, \tag{30}$$

$$\begin{cases} \text{(Case1)}: & \tilde{\theta}(0) = \tilde{\theta}(1) = 0\,, \\ \text{(Case2)}: & \dfrac{\mathrm{d}\tilde{\theta}}{\mathrm{d}z}(0) = 0,\ \tilde{\theta}(1) = 0\,. \end{cases} \tag{31}$$

By solving the eigenvalue problem consisting of (25)−(31), we can obtain the growth rate as a function of the Rayleigh number Ra and the disturbance wavenumber σ. We are particularly interested in the contour of zero growth, which is called the "neutral curve". From the neutral curves, we can determine the critical Rayleigh number and the critical wavenumber, which are the critical conditions for the onset of instability. These results will be discussed in Section 4.

3.2 Numerical Method

The spectral method is chosen to solve the eigenvalue problem posed in Section 3.1 because it is well known that spectral methods can easily provide high spatial resolution (Canuto *et al.*, 1988). To employ such method, a Gauss–Lobatto grid with 35 gridpoints is used in the z direction and associated Chebyshev expansions for the tilde quantities are applied to discretize the governing equations (25)−(28) and the boundary conditions (29) −(31). Based on the property of the Chebyshev expansion, the derivatives in the eigenvalue system can be replaced by the so-called "derivative matrices" (Canuto *et al.*, 1988), and eventually the eigenvalue system becomes a large linear algebraic system that has the matrix form:

$$A_1\hat{x} = \omega A_2\hat{x}\,.$$

Here A_1 and A_2 are matrices in which the effects of the governing equations and the boundary conditions are incorporated, and $\hat{x}$ is a vector consisting of the values of the tilde quantities at every gridpoint. This is called a generalized eigenvalue problem. Many packages, such as EISPACK, IMSL, and NAG, have routines to treat this kind of problem. An inversed iteration method (Press *et al.*, 1996) is employed in our current numerical code.

To determine the components of the matricies A_1 and A_2, the following items need to be specified: Prandtl number (Pr), internal heating parameter (H), horizontal velocity boundary conditions (rigid or stress–free), thermal boundary conditions (isothermal or insulating), and the buoyancy factor profile (constant or variable). For each given set of parameter values, we first solve the associated eigenvalue problem for $\sigma \in [0.0001, 20.0]$ and $\mathrm{Ra} \in [100.0, 25000.0]$ to determine the neutral curve and the critical conditions. The eigenfunctions for $\tilde{u}_1$, $\tilde{u}_3$, $\tilde{p}$, and $\tilde{\theta}$ corresponding to the critical conditions are then calculated. These eigenfunctions are normalized in such a way that the resultant normalized kinetic energy for the disturbances over the whole layer becomes unity, i.e.

$$\int_0^1 \left(\tilde{u}_1^2 + \tilde{u}_3^2\right) \mathrm{d}z = 1\,. \tag{32}$$

The shape of the normalized $\tilde{u}_3$ eigenfunction is then examined, so that the location and the magnitude of the extremum can be determined.

4 Results and Discussion of Stability Analysis

For the present stability study, we restrict our computation to the case where the thermal boundary conditions are isothermal on both boundaries. The main general results are:

(i) The real part of the eigenvalue ω is always zero, implying that the disturbances are not oscillatory in time. Thus, ω is exactly zero on the neutral curve.

(ii) The complex eigenfunctions for $\tilde{u}_1$ and $\tilde{p}$ are purely imaginary, while those for $\tilde{u}_3$ and $\tilde{\theta}$ are purely real.

(iii) The critical conditions for the eigenvalue and eigenfunctions are all independent of Pr.

Before applying our numerical scheme to the variable buoyancy factor (VB) cases, we first carry out a brief study for the effects of H and the velocity boundary conditions on the onset of instability in the presence of a constant buoyancy factor (CB). Such a study can help us evaluate the roles played by H and the velocity boundary conditions. In addition, it is important to establish a baseline of reference so that a meaningful comparison with the results of variable buoyancy factor cases can be constructed.

4.1 The Effect of H

For this study, we chose SS for the horizontal velocity boundary conditions — see equation (29) — and CB cases for $H = 0, 1.0, \pm 2.0, \pm 5.0$ have been calculated. The reason that we chose to calculate such cases is to see if around $H = 2.0$ there is a significant change in the critical conditions. The data generated from the neutral stability curve are shown in Table I, where $(\mathrm{Ra})_{\mathrm{cr}}$ and σ_{cr} are the critical Rayleigh number and the critical wavenumber, respectively. Table I shows that the critical wavenumber is independent of H, and the critical Rayleigh number decreases slowly as $|H|$ increases. The rate at which $(\mathrm{Ra})_{\mathrm{cr}}$ decreases, is smaller as $|H|$ decreases (see Figure 1).

The shapes of the $\tilde{u}_3$ and $\tilde{\theta}$ eigenfunction are shown in Figures 2 and 3, respectively. From these figures, we see that H has very little effect on the eigenfunctions. The eigenfunctions seem to follow a shape of half a sine cycle, with its maximum point located at the center ($z = 0.5$). As $|H|$ increases from 0 to 5.0, the maximum value

H	0	1.0	± 2.0	± 5.0
$(\mathrm{Ra})_{\mathrm{cr}}$	657.51	656.69	654.26	638.21
σ_{cr}	2.221	2.221	2.221	2.221

Table I. Effect of H on the critical conditions

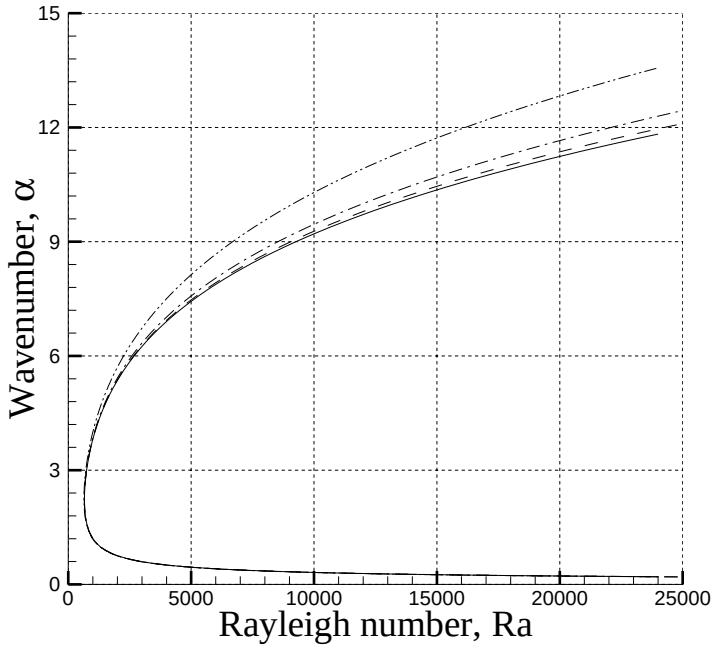

Figure 1. Effect of $|H|$ on the neutral curve (The solid line is for $|H|$=0, the dashed line is for $|H|$=1.0, the dashdot line is for $|H|$=2.0, and the dashdotdot line is for $|H|$=5.0).

of $\tilde{u}_3$ shows only a 0.18% reduction (from 0.8159 to 0.8144). Furthermore, when H is positive, the maxima of the eigenfunctions of $\tilde{u}_3$ and $\tilde{\theta}$ shift upward from the centerline.

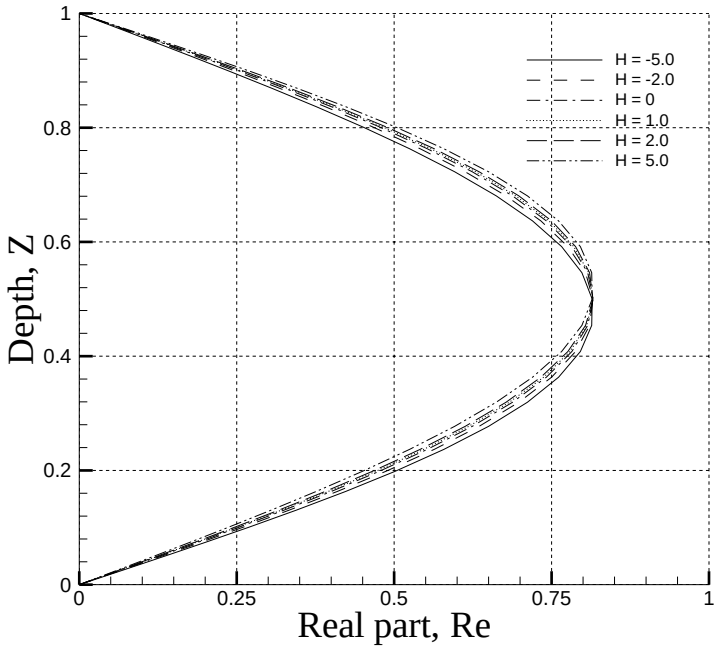

Figure 2. Effect of $|H|$ on $\tilde{u}_3$ eigenfunction.

In this investigation, we consider a CB case only; therefore

$$B(z) = B(1-z)\,.$$

It can be proved, based on our formulation, the following relationships exist between the case of $+H$ and the case of $-H$ for both the RR and the SS cases:

$$\begin{cases} \sigma_{-H} = \sigma_{+H}\,, \\ \omega_{-H} = \omega_{+H}\,, \\ (\mathrm{Ra})_{-H} = (\mathrm{Ra})_{+H}\,, \\ (\tilde{u}_1)_{-H}(z) = (\tilde{u}_1)_{+H}(1-z)\,, \\ (\tilde{u}_3)_{-H}(z) = -(\tilde{u}_3)_{+H}(1-z)\,, \\ \tilde{p}_{-H}(z) = \tilde{p}_{+H}(1-z)\,, \quad \text{and} \\ \tilde{\theta}_{-H}(z) = -\tilde{\theta}_{+H}(1-z)\,. \end{cases}$$

This means that the case of $-H$ is mathematically equivalent to the case of $+H$.

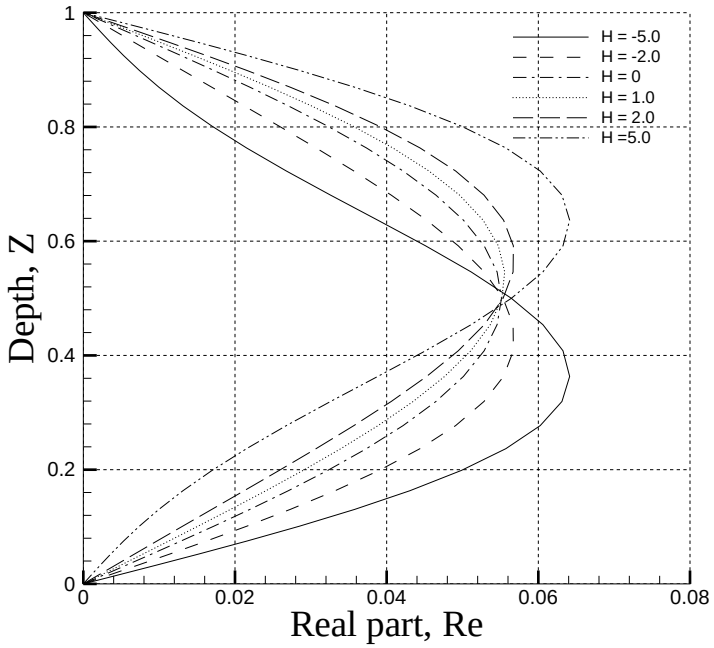

Figure 3. Effect of $|H|$ on $\tilde{\theta}$ eigenfunction.

4.2 The Effect of the Velocity Boundary Conditions

For this study, we chose CB and $H = 0$. Cases for RR, RS, SR, and SS velocity boundary conditions are calculated. Results about the growth rate contours (Table II and Figure 4) indicate that the SS case gives the lowest $(\mathrm{Ra})_{\mathrm{cr}}$ and the smallest σ_{cr}, the RR case gives the largest $(\mathrm{Ra})_{\mathrm{cr}}$ and the biggest σ_{cr}, whereas the RS case and the SR case have exactly the same critical conditions. These results are physically understandable. A rigid boundary poses friction on a flow and leads to shorter-wavelength flow circulations, which imply a higher value for both σ_{cr} and $(\mathrm{Ra})_{\mathrm{cr}}$ as compared with the corresponding effects due to a stress–free boundary.

B.C.	RR	RS	SR	SS
$(\mathrm{Ra})_{\mathrm{cr}}$	1707.76	1100.65	1100.65	675.51
σ_{cr}	3.117	2.681	2.681	2.221

Table II. Effect of velocity boundary conditions on the critical conditions

Since we considered the CB case and no internal heating in this investigation, we have

$$B(z) = B(1-z), \quad H = 0\,.$$

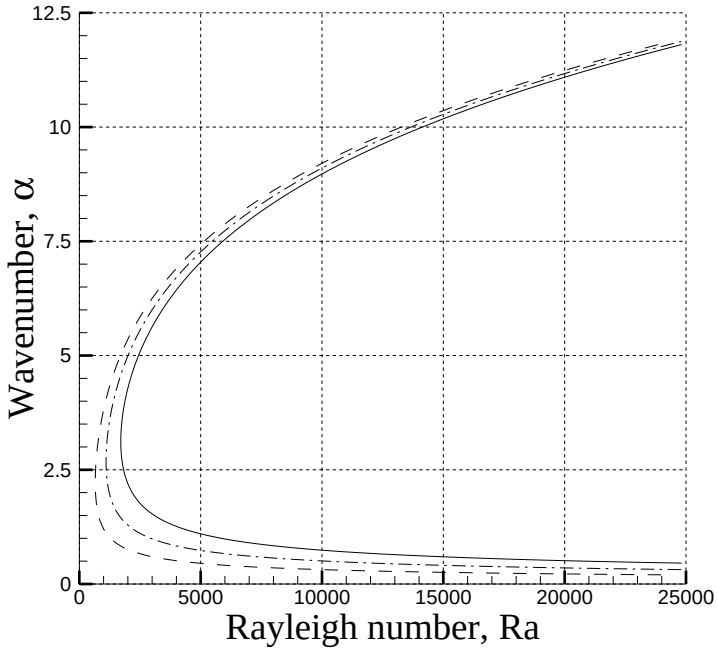

Figure 4. Effect of velocity boundary conditions on the neutral curve (The solid line is for the RR case, the dashed line is for the SS case, and the dashdot line is for the RS/SR cases).

It can be proved that the following relationships exist between the RS case and the SR case:

$$\begin{cases} \sigma_{_{RS}} = \sigma_{_{SR}} \ , \\ \omega_{_{RS}} = \omega_{_{SR}} \ , \\ (\mathrm{Ra})_{_{RS}} = (\mathrm{Ra})_{_{SR}} \ , \\ (\tilde{u}_1)_{_{RS}}(z) = (\tilde{u}_1)_{_{SR}}(1-z) \ , \\ (\tilde{u}_3)_{_{RS}}(z) = -(\tilde{u}_3)_{_{SR}}(1-z) \ , \\ \tilde{p}_{_{RS}}(z) = \tilde{p}_{_{SR}}(1-z) \, , \quad \text{and} \\ \tilde{\theta}_{_{RS}}(z) = -\tilde{\theta}_{_{SR}}(1-z) \, . \end{cases}$$

This means that the RS case is mathematically equivalent to the SR case.

The $\tilde{u}_3$ eigenfunctions corresponding to different velocity boundary conditions are shown in Figure 5. It is found that the $\tilde{u}_3$ eigenfunction is asymmetric with respect to the centerline if the two velocity boundary conditions are not identical. The peak of this eigenfunction is skewed towards the stress–free boundary.

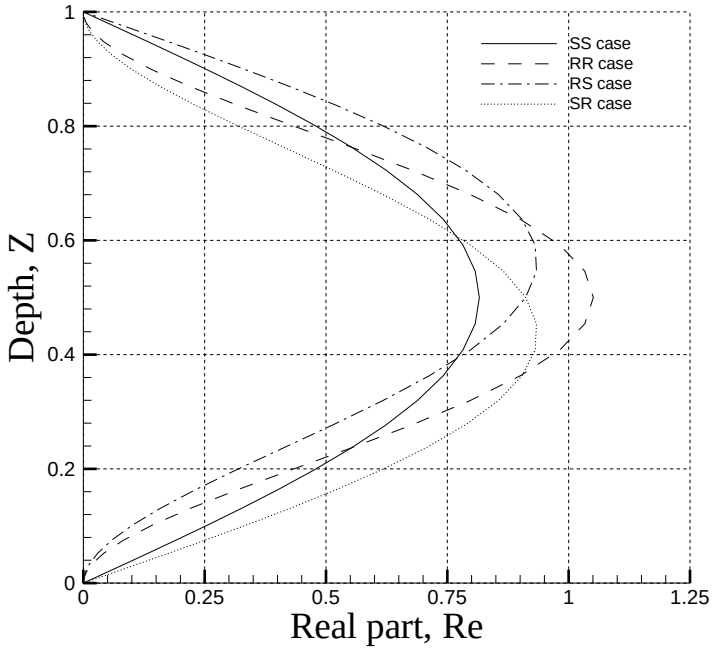

Figure 5. Effect of velocity boundary conditions on the $\tilde{u}_3$ eigenfunction.

Based on the above study for the CB cases, neither H nor Pr plays any significant role in the linear stability of the present convective system. Therefore, for the investigations of the VB cases, we will set $H = 0$, and focus our attention on the effects of

variable buoyancy factor only. Several variable buoyancy factor profiles are used in this study. These include two linear profiles, a parabolic profile, a sinusoidal profile, and a more realistic profile derived from Stacey's work (1992) for the Earth. Physically these variable buoyancy factor profiles can be implemented by either the variation of gravity field or the variation of thermal expansion coefficient or some combinations of these two variations. Results of the VB cases are discussed in the following subsections.

4.3 The Effect of a Linear Buoyancy Factor Profile with Reference B_0 Tied to the Bottom (VB–LB)

First we want to investigate how a monotonically changing buoyancy factor profile affects the stability of the system. Among the monotonic buoyancy factor profiles, we choose to start with a simple case, the linear profile. For this study, the buoyancy factor profile is chosen to be

$$B(z) = 1 + \epsilon_1 z \,,$$

where ϵ_1 is a constant representing the rate of vertical change of the buoyancy factor. The reference buoyancy factor B_0 is set at the bottom boundary. Whether the buoyancy factor increases or decreases with z depends on the sign of ϵ_1. Here the RR and SS cases have been studied for ϵ_1 ranging from -0.95 to 1.20.

Data for the growth rate contours (Figures 6) indicate that the critical Rayleigh number decreases as ϵ_1 increases, and the rate of decrease also decreases as ϵ_1 increases — notice that in Figure 6 the slope of the $(\mathrm{Ra})_{\mathrm{cr}}$ vs. ϵ_1 curve is always negative, but it increases as ϵ_1 increases) — i.e.

$$\frac{\mathrm{d}}{\mathrm{d}\epsilon_1}(\mathrm{Ra})_{\mathrm{cr}} < 0 \,, \quad \frac{\mathrm{d}^2}{\mathrm{d}\epsilon_1^2}(\mathrm{Ra})_{\mathrm{cr}} > 0 \,.$$

Therefore, for $\epsilon_1 > 0$, lower critical Rayleigh numbers are found when compared with the CB case. Conversely, for $\epsilon_1 < 0$, higher critical Rayleigh numbers are obtained. These trends hold for both the SS and the RR cases. On the other hand, the critical wavenumber is independent of ϵ_1, i.e. it is 2.221 for all SS cases and 3.117 for all RR cases (Figures 7 and 8).

As to the $\tilde{u}_3$ eigenfunction (Figures 9 and 10), the maximum point is almost always at the middle, except in the case of very low ϵ_1 (i.e.$\epsilon_1 = -0.95$). The magnitude of the maximum point does not depend on ϵ_1. However, the shape of the $\tilde{u}_3$ eigenfunction is slightly affected by the value of ϵ_1. For example, when $\epsilon_1 = 0$, a symmetric profile is obtained. When $\epsilon_1 > 0$, the profile is skewed towards the upper half, and when $\epsilon_1 < 0$, it is skewed in the opposite direction.

To investigate the effect of reference buoyancy factor location on the stability of the system, we studied cases where the reference buoyancy factor is tied to the top

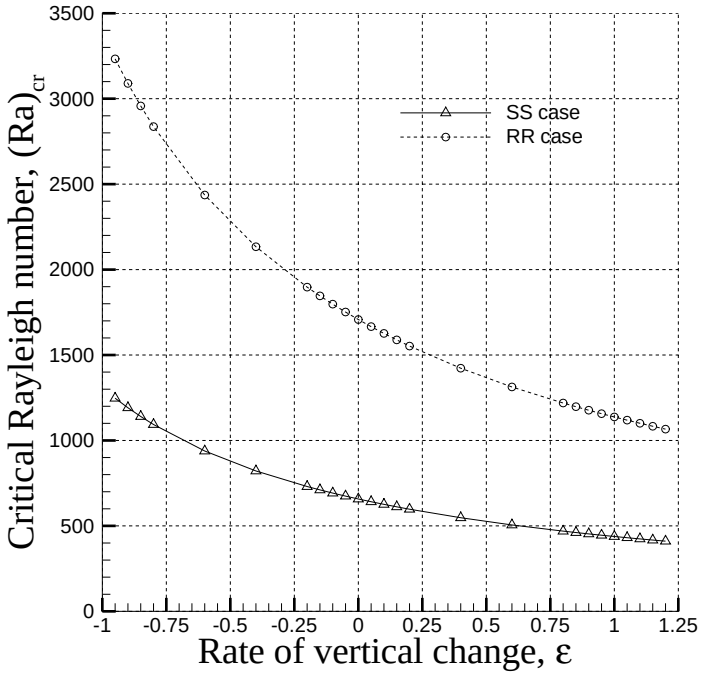

Figure 6. Effect of VB–LB on the critical Rayleigh number in the SS and RR cases.

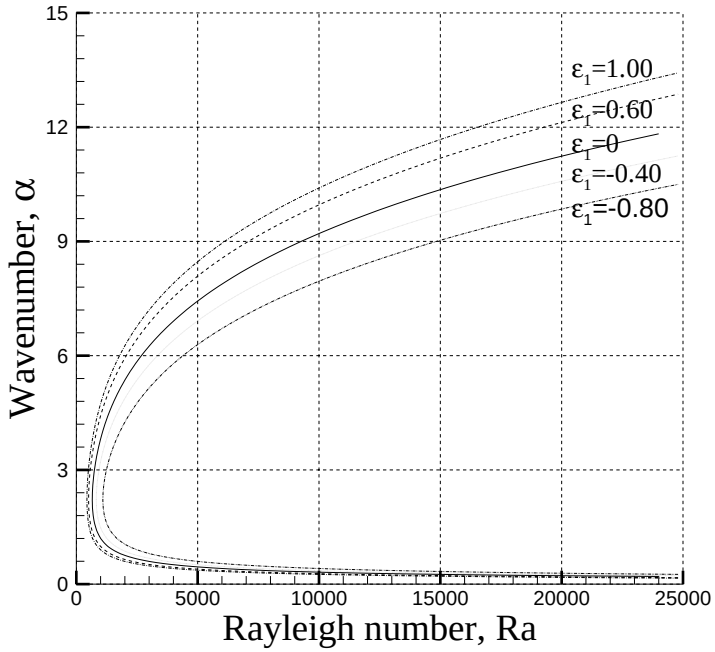

Figure 7. Effect of VB–LB on the neutral curve in the SS case.

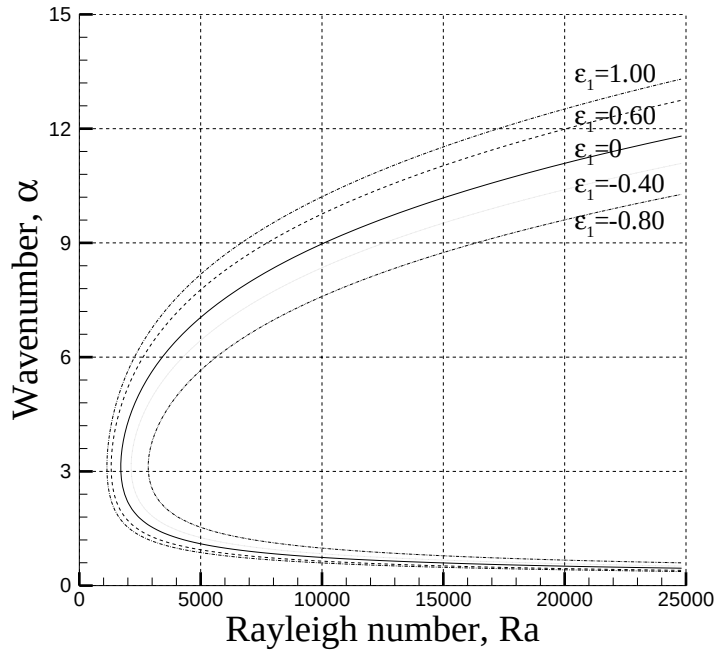

Figure 8. Effect of VB–LB on the neutral curve in the RR case.

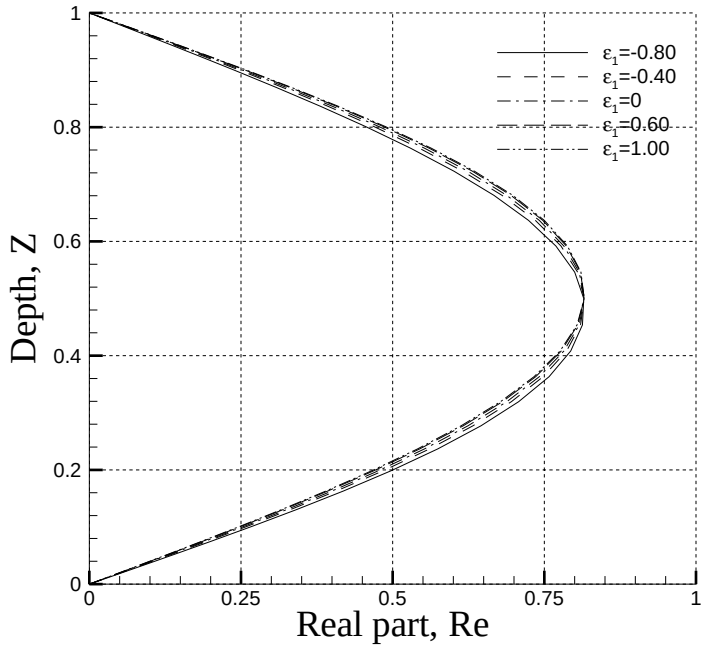

Figure 9. Effect of VB–LB on the $\tilde{u}_3$ eigenfunction in the SS case.

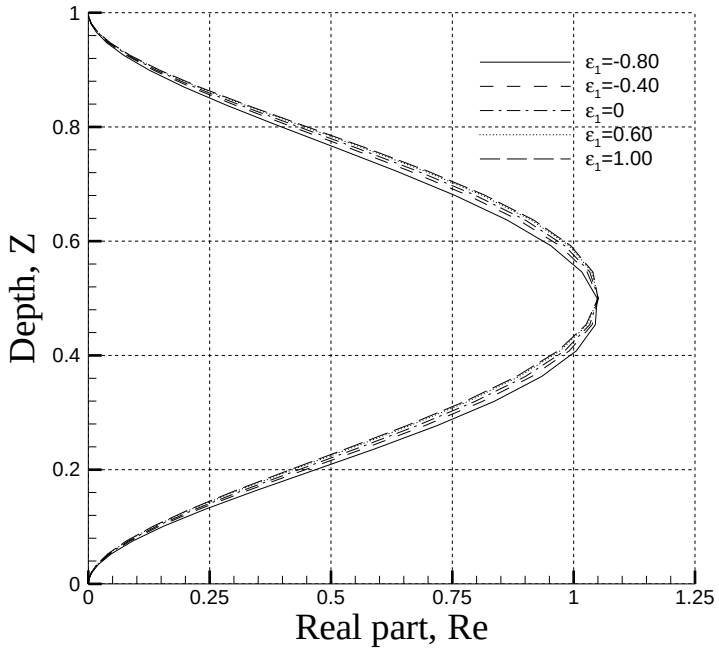

Figure 10. Effect of VB–LB on the $\tilde{u}_3$ eigenfunction in the RR case.

boundary (VB–LT) as well. In other words, for that study, the buoyancy factor profile is chosen to be

$$B(z) = 1 + \epsilon_1 (z - 1) \, .$$

Both the SS and RR cases have been tested for several values of ϵ_1. It turns out that, since we considered no internal heating, the following relationships exist between VB–LT case of given ϵ_1 and VB–LB case of given $-\epsilon_1$:

$$\begin{cases} \sigma_{LT,\epsilon_1} = \sigma_{LB,-\epsilon_1} \ , \\ \omega_{LT,\epsilon_1} = \omega_{LB,-\epsilon_1} \ , \\ (\mathrm{Ra})_{LT,\epsilon_1} = (\mathrm{Ra})_{LB,-\epsilon_1} \ , \\ (\tilde{u}_1)_{LT,\epsilon_1}(z) = (\tilde{u}_1)_{LB,-\epsilon_1}(1-z) \, , \\ (\tilde{u}_3)_{LT,\epsilon_1}(z) = -(\tilde{u}_3)_{LB,-\epsilon_1}(1-z) \, , \\ \tilde{p}_{LT,\epsilon_1}(z) = \tilde{p}_{LB,-\epsilon_1}(1-z) \, , \quad \text{and} \\ \tilde{\theta}_{LT,\epsilon_1}(z) = -\tilde{\theta}_{LB,-\epsilon_1}(1-z) \, . \end{cases}$$

This means that VB–LT case of given ϵ_1 is mathematically equivalent to VB–LB case of $-\epsilon_1$.

4.4 The Effect of a Parabolic Buoyancy Factor Profile (Para–VB)

Beginning with this subsection, we examine the effects of some non–monotonic buoyancy factor profiles. First of all, we want to see how non–monotonic buoyancy factor profiles with only one local extremum affect the stability of the system. Actually, we chose the following parabolic profile for our investigation:

$$B(z) = 1 - 4\epsilon_2 z + 4\epsilon_2 z^2 \,,$$

where the constant ϵ_2 is called "deficit parameter" in this paper. It stands for the deficit percentage of the buoyancy factor at the middle of the domain with respect to the reference value. Both the SS and RR cases have been studied for several values of ϵ_2 in the range $-0.80 < \epsilon_2 < 1$.

Data for the growth rate contours (Figure 11) indicate that the critical Rayleigh number increases as ϵ_2 increases, and the rate of increase also increases as ϵ_2 increases — notice that in Figure 11 the slope of the $(\mathrm{Ra})_{\mathrm{cr}}$-$\epsilon_2$ curve is always positive, but it increases as ϵ_2 increases) — i.e.

$$\frac{\mathrm{d}}{\mathrm{d}\epsilon_2}(\mathrm{Ra})_{\mathrm{cr}} > 0 \,, \quad \frac{\mathrm{d}^2}{\mathrm{d}\epsilon_2^2}(\mathrm{Ra})_{\mathrm{cr}} > 0 \,.$$

Therefore, compared with a CB case, buoyancy factor deficits ($\epsilon_2 > 0$) increase the critical Rayleigh number. The larger the deficit, the higher the critical Rayleigh number becomes. Conversely, buoyancy factor gains ($\epsilon_2 < 0$) yield lower critical Rayleigh numbers. On the other hand, for a wide range of deficit parameter ϵ_2 that we have tested ($-0.8 \le \epsilon_2 \le 0.8$), the critical wavenumber remains constant, i.e. 2.221 for all SS cases and 3.117 for all RR cases (Figures 12 and 13).

As to the $\tilde{u}_3$ eigenfunction, it is symmetric with respect to the centerline for both the SS and RR cases, and the deficit parameter ϵ_2 almost has no effect on its shape and magnitude (Figures 14 and 15).

4.5 The Effect of a Sinusoidal Buoyancy Factor Profile (Sine–VB)

We next examine the effects of possible multiple local extrema for the dynamics of the flow system. For this case, the buoyancy factor profile is chosen to be

$$B(z) = 1 - \epsilon_3 \sin(2\pi N z) \,,$$

where the parameters ϵ_3 and $2\pi N$ describe, respectively, the amplitude and the wavenumber of the deviation from a constant buoyancy factor profile. Both the SS and RR cases have been studied for several values of ϵ_3 and N.

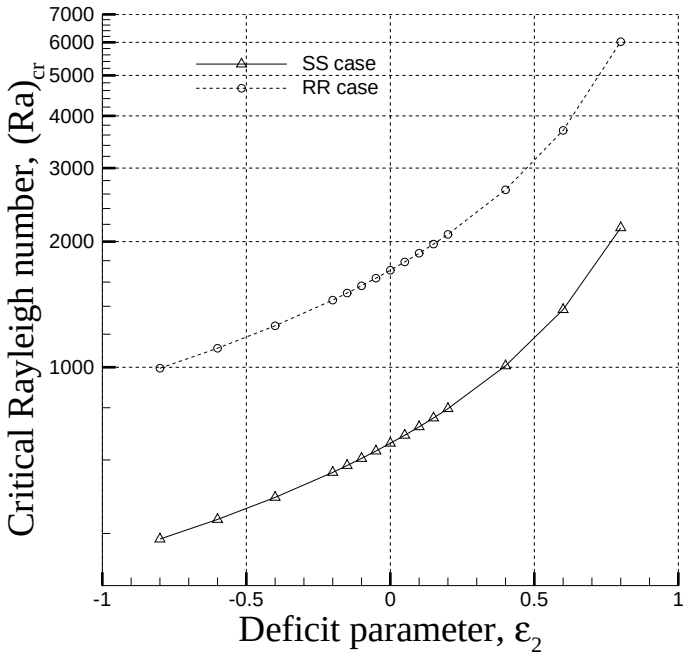

Figure 11. Effect of para–VB on critical Rayleigh number in the SS and RR cases.

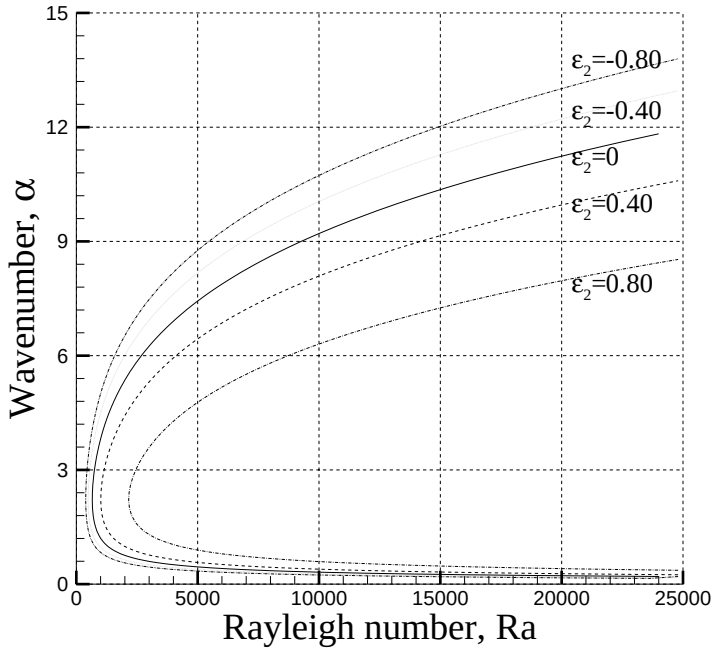

Figure 12. Effect of para–VB on the neutral curve in the SS case.

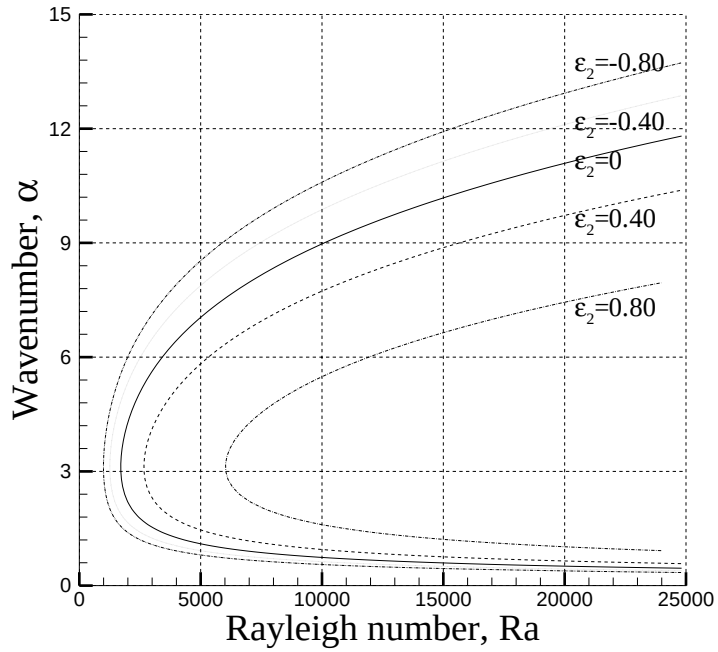

Figure 13. Effect of para–VB on the neutral curve in the RR case.

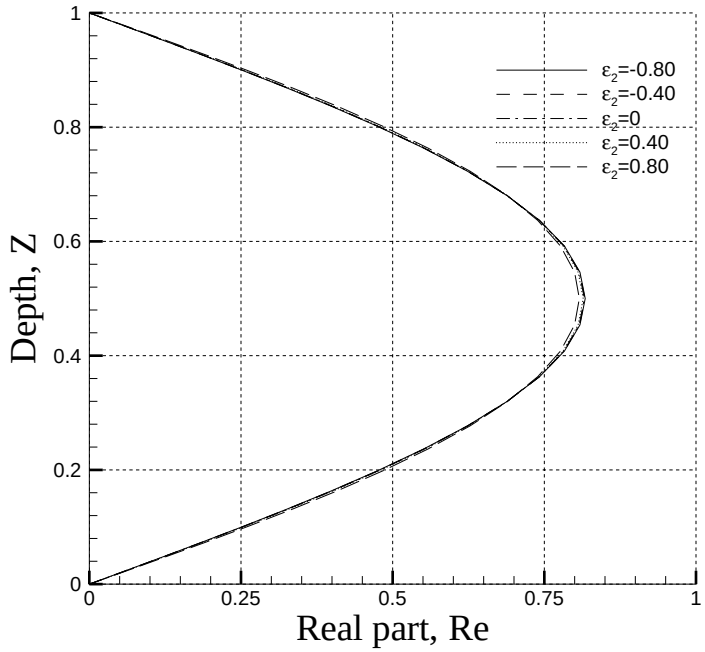

Figure 14. Effect of para–VB on the $\tilde{u}_3$ eigenfunction in the SS case.

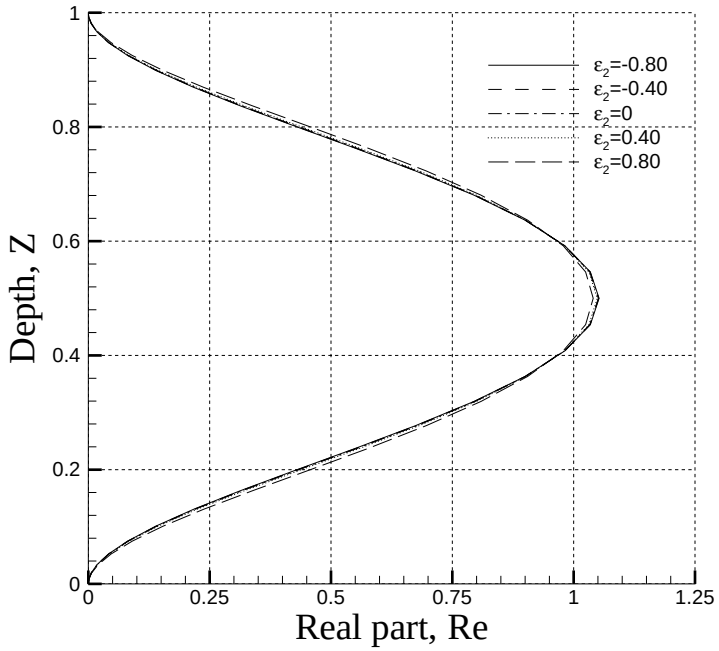

Figure 15. Effect of para–VB on the $\tilde{u}_3$ eigenfunction in the RR case.

Results of the critical conditions (Tables III – VI) indicate that the critical Rayleigh number decreases with increasing ϵ_3 and increases with N. For a given ϵ_3, the critical Rayleigh number approaches that of a CB case as N increases. On the other hand, the critical wavenumber remains unchanged. Furthermore, the critical Rayleigh numbers are not much different from that of a CB case, even though the buoyancy factor profiles differ significantly. This result suggests that in this case the average buoyancy factor across the whole layer plays the most important role in determining the stability behavior of the system. It is also noticed that, for $N \geq 3$, the corresponding critical Rayleigh numbers are almost the same as that of a CB case, even for a large–amplitude deviation such as $\epsilon_3 = 0.9$. As to the $\tilde{u}_3$ eigenfunction, positive ϵ_3 makes the $\tilde{u}_3$ eigenfunction skew towards the upper half, because the upper half has a higher buoyancy factor and, therefore, tends to become unstable more easily. Similarly, negative ϵ_3 makes the curve shift towards the lower half (Figures 16 and 17). However, for $N \geq 3$, the eigenfunction differs only slightly from that of a CB case. This result, combined with the effect of N on the critical Rayleigh number, implies that a sine–VB profile can only affect the linear stability of the system when $N = 1, 2$.

Finally, since we considered no internal heating in this investigation, it can be proved, based on our formulation, that the following relationships exist between the

ϵ_3	0	0.05	0.10	0.15	0.20	0.25
$(\mathrm{Ra})_{\mathrm{cr}}$	657.51	657.48	657.40	657.25	657.05	656.78
σ_{cr}	2.221	2.221	2.221	2.221	2.221	2.221
ϵ_3	0.30	0.35	0.40	0.50	0.60	0.70
$(\mathrm{Ra})_{\mathrm{cr}}$	656.46	656.09	655.65	654.62	653.36	651.89
σ_{cr}	2.221	2.221	2.221	2.221	2.221	2.221
ϵ_3	0.75	0.80	0.85	0.90		
$(\mathrm{Ra})_{\mathrm{cr}}$	651.07	650.21	649.29	648.32		
σ_{cr}	2.221	2.221	2.221	2.221		

Table III. Effect of ϵ_3 on the critical conditions in the SS case ($N = 1$)

N	1	2	3	4	5	6	7
$(\mathrm{Ra})_{\mathrm{cr}}$	648.32	656.58	657.46	657.50	657.51	657.51	657.51
σ_{cr}	2.221	2.221	2.221	2.221	2.221	2.221	2.221

Table IV. Effect of N on the critical conditions in the SS case ($\epsilon_3 = 0.9$)

ϵ_3	0	0.05	0.10	0.15	0.20	0.25
$(\mathrm{Ra})_{\mathrm{cr}}$	1707.76	1707.65	1707.21	1706.52	1705.56	1704.32
σ_{cr}	3.117	3.117	3.117	3.117	3.117	3.117
ϵ_3	0.30	0.35	0.40	0.50	0.60	0.70
$(\mathrm{Ra})_{\mathrm{cr}}$	1702.81	1701.04	1699.01	1694.17	1688.34	1681.54
σ_{cr}	3.117	3.117	3.117	3.117	3.117	3.117
ϵ_3	0.75	0.80	0.85	0.90		
$(\mathrm{Ra})_{\mathrm{cr}}$	1677.80	1673.84	1669.66	1665.28		
σ_{cr}	3.117	3.117	3.117	3.117		

Table V. Effect of ϵ_3 on the critical conditions in the RR case ($N = 1$)

N	1	2	3	4	5	6	7
$(\mathrm{Ra})_{\mathrm{cr}}$	1665.28	1697.16	1707.29	1707.70	1707.75	1707.76	1707.76
σ_{cr}	3.117	3.117	3.117	3.117	3.117	3.117	3.117

Table VI. Effect of N on the critical conditions in the RR case ($\epsilon_3 = 0.9$)

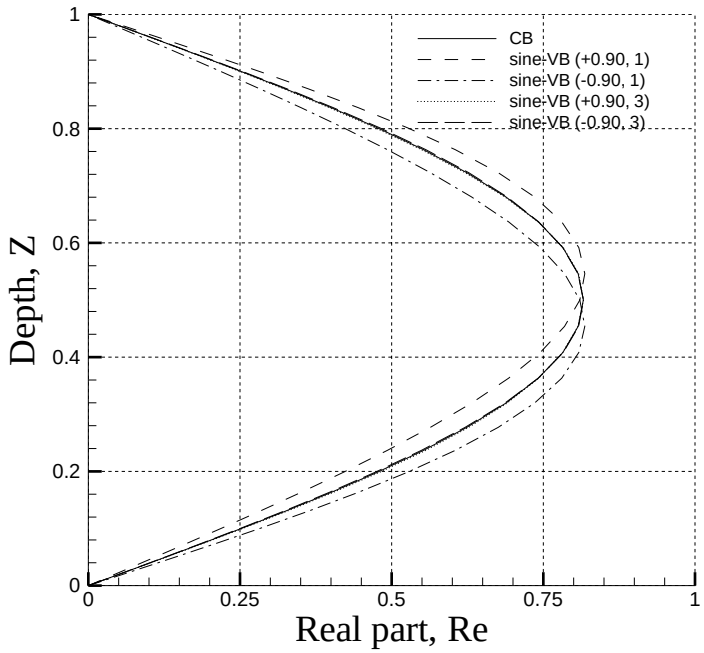

Figure 16. Effect of sine–VB on the $\tilde{u}_3$ eigenfunction in the SS case.

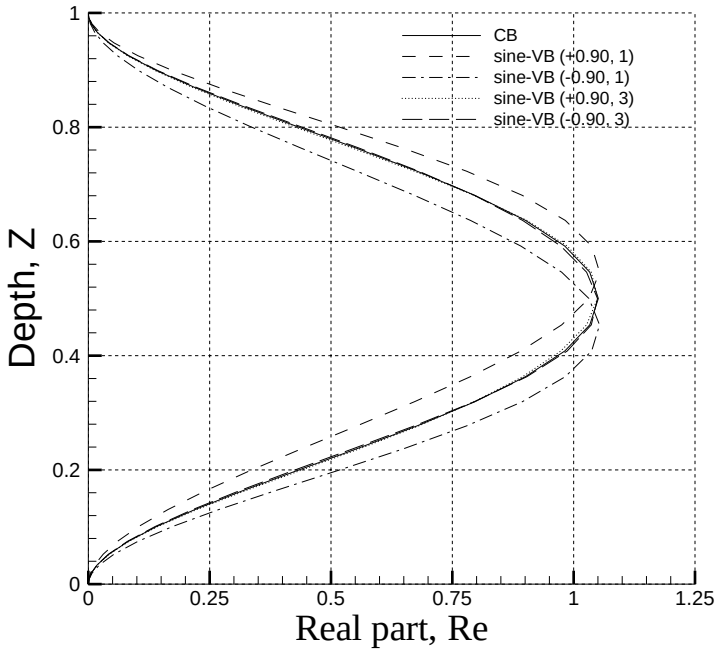

Figure 17. Effect of sine–VB on the $\tilde{u}_3$ eigenfunction in the RR case.

sine–VB case of given (ϵ_3, N) and the sine–VB case of $(-\epsilon_3, N)$:

$$\begin{cases} \sigma_{\epsilon_3,N} = \sigma_{-\epsilon_3,N} \ , \\ \omega_{\epsilon_3,N} = \omega_{-\epsilon_3,N} \ , \\ (\mathrm{Ra})_{\epsilon_3,N} = (\mathrm{Ra})_{-\epsilon_3,N} \\ (\tilde{u}_1)_{\epsilon_3,N}(z) = (\tilde{u}_1)_{-\epsilon_3,N}(1-z) \, , \\ (\tilde{u}_3)_{\epsilon_3,N}(z) = -(\tilde{u}_3)_{-\epsilon_3,N}(1-z) \, , \\ \tilde{p}_{\epsilon_3,N}(z) = \tilde{p}_{-\epsilon_3,N}(1-z) \, , \quad \text{and} \\ \tilde{\theta}_{\epsilon_3,N}(z) = -\tilde{\theta}_{-\epsilon_3,N}(1-z) \, . \end{cases}$$

This means that the sine–VB case of given (ϵ_3, N) is mathematically equivalent to the sine–VB of $(-\epsilon_3, N)$.

4.6 The Effect of a "Realistic" Buoyancy Factor Profile (Real-VB)

For this study, the buoyancy factor profile is chosen to follow Stacey's profile (1992) (Figure 18). Here the RR, RS, SR, and SS cases have been studied and compared with their counterparts in the CB case.

Results of the critical conditions (Table VII) indicate that when compared with the CB case, the critical Rayleigh number for the realistic VB case is slightly lower in all four cases. The critical wavenumber remains the same, however. Furthermore, since the realistic buoyancy factor profile is not symmetric with respect to the centerline of the fluid layer, the RS case and the SR case are no longer mathematically equivalent to each other. However, the deviation from mathematical equivalence is quite small (Table VII and Figure 19).

	CB				real-VB			
	RR	RS	SR	SS	RR	RS	SR	SS
$(\mathrm{Ra})_{\mathrm{cr}}$	1707.76	1100.65	1100.65	657.51	1692.73	1089.66	1090.48	650.95
σ_{cr}	3.117	2.681	2.681	2.221	3.117	2.681	2.681	2.221

Table VII. Effect of real–VB on the critical conditions

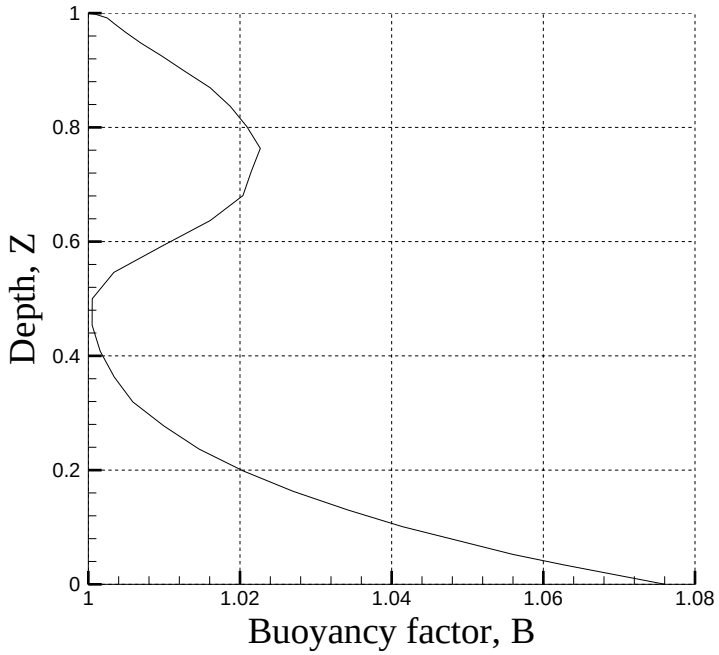

Figure 18. Realistic variable buoyancy factor profile (reproduced from Stacey 1992).

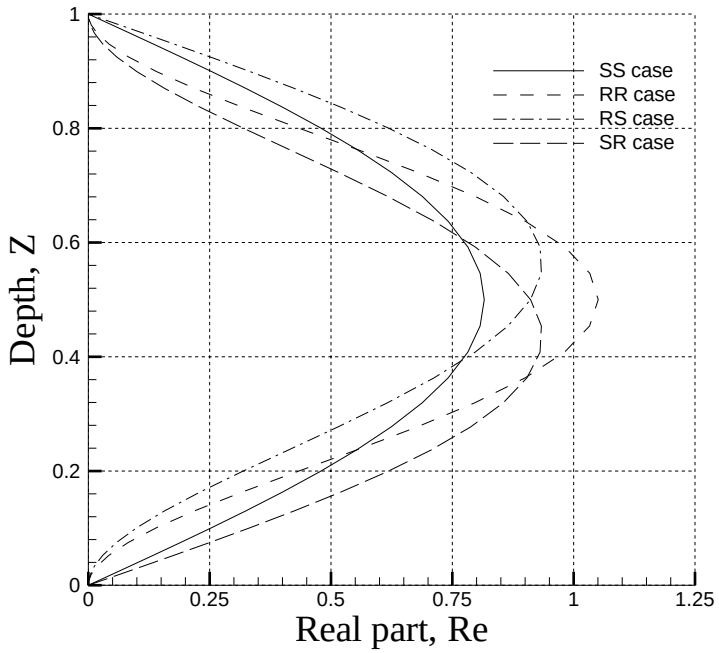

Figure 19. Effect of velocity boundary conditions on the $\tilde{u}_3$ eigenfunction in the real–VB case.

4.7 Estimation of the Effects of Variable Buoyancy Factor on the Critical Conditions

On the basis of previous discussions, it appears that the critical wavenumber is independent of the buoyancy factor profiles when the buoyancy factor keeps the same sign in the entire domain. It is of interest to examine if there is a general relationship between a buoyancy factor profile and the corresponding critical Rayleigh number. We will evaluate the relationship in terms of the following statistical quantities for a given variable buoyancy factor profile $B(z)$:

1. $B_{\rm av} = \int_0^1 B(z)\mathrm{d}z$, the mean buoyancy factor.
2. $B_{\rm sd} = \int_0^1 [B(z) - B_{\rm av}]^2 \, \mathrm{d}z$, the standard deviation of the buoyancy factor.
3. $B_{\rm sk} = \int_0^1 [B(z) - B_{\rm av}]^3 \, \mathrm{d}z$, the third–order moment of the buoyancy factor.
4. $B_{\rm fl} = \int_0^1 [B(z) - B_{\rm av}]^4 \, \mathrm{d}z$, the fourth–order moment of the buoyancy factor.

Therefore, for the various types of the buoyancy factor profiles we discussed before, we obtain the results given in Table VIII.

Type	$B(z)$	$B_{\rm av}$	$B_{\rm sd}$	$B_{\rm sk}$	$B_{\rm fl}$
Linear	$1 + \epsilon_1 z$	$1 + \frac{1}{2}\epsilon_1$	$\frac{1}{12}\epsilon_1^2$	0	$\frac{1}{80}\epsilon_1^4$
Parabolic	$1 - 4\epsilon_2 z + 4\epsilon_2 z^2$	$1 - \frac{2}{3}\epsilon_2$	$\frac{4}{45}\epsilon_2^2$	$\frac{16}{945}\epsilon_2^3$	$\frac{16}{945}\epsilon_2^4$
Sinusoidal	$1 + \epsilon_3 \sin(2\pi N z)$	1	$\frac{1}{2}\epsilon_3^2$	0	$\frac{3}{8}\epsilon_3^4$
"Realistic"	Discrete data	1.0174	2.7663 e−4	7.1202 e−6	3.9624 e−7

Table VIII. The statistical features of the variable buoyancy factor profiles

We assume that by using up to the third–order moment we can capture the effect of variable buoyancy factor on the critical Rayleigh number. In other words, we express the critical Rayleigh number as a function of $B_{\rm av}$, $B_{\rm sd}$ and $B_{\rm sk}$. Furthermore, we assume that the effects of $B_{\rm av}$, $B_{\rm sd}$, and $B_{\rm sk}$ on the critical Rayleigh number do not couple with each other, i.e.

$$(\mathrm{Ra})_{\rm cr} = F\left(B_{\rm av}, B_{\rm sd}, B_{\rm sk}\right) = f_1(B_{\rm av}) f_2(B_{\rm sd}) f_3(B_{\rm sk}) \,, \tag{33}$$

where F, f_1, f_2, and f_3 are functions to be determined, and $F(1,0,0) = f_1(1)f_2(0)f_3(0)$ equals the critical Rayleigh number in the CB case, i.e. 657.51 for the SS case and 1707.76 for the RR case. These assumptions will be justified later in this subsection.

Since a sinusoidal buoyancy factor profile has the same $B_{\rm av}$ and $B_{\rm sk}$ values as the constant buoyancy factor profile, the only factor that affects the critical Rayleigh number in a sinusoidal buoyancy factor field is $B_{\rm sd}$. By analyzing the results for $N = 1$ that we obtained in Section 4.6, we have the following form for f_2 based on the least–square–error algorithm:

$$f_2(x) = \begin{cases} f_2(0)\,(1 - 0.0621x) & \text{for RR case} \\ f_2(0)\,(1 - 0.0347x) & \text{for SS case} \end{cases} \tag{34}$$

Similarly, for the linear buoyancy factor profile, only $B_{\rm av}$ and $B_{\rm sd}$ affect the critical Rayleigh number, where the effect of $B_{\rm sd}$ is expressed by (34). Again, based on the least–square–error algorithm, we obtain the following bestfit for f_1 for both the RR and the SS cases:

$$f_1(x) = f_1(1)\,x^{-0.998}\,, \tag{35}$$

and, using (33)−(35) to analyze the critical Rayleigh numbers in the parabolic buoyancy factor fields (Section 4.5), we obtain the following bestfit for f_3:

$$f_3(x) = \begin{cases} f_3(0)\ \left[0.9118 + 0.0882\exp\left(10.237x^{1/3}\right)\right] & \text{for RR case} \\ f_3(0)\ \left[0.9138 + 0.0862\exp\left(9.499x^{1/3}\right)\right] & \text{for SS case} \end{cases} \tag{36}$$

It should be noted that $f_1(1)$, $f_2(0)$, and $f_3(0)$ in (34)−(36) can not be completely determined in this investigation. However, according to (33), these three numbers must satisfy the following constraint:

$$f_1(1)f_2(0)f_3(0) = \begin{cases} 1707.76 & \text{for RR case} \\ 657.51 & \text{for SS case} \end{cases} \tag{37}$$

We used (33)−(37) to estimate the critical Rayleigh numbers for all the variable buoyancy factor profiles we studied and compared them with the corresponding results from the linear stability analysis. For the 58 cases we have studied, the relative difference between the estimated value and the computed values is $(1.418 \pm 7.037) \times 10^{-3}$ for the RR case, and $(1.314 \pm 5.462) \times 10^{-3}$ for the SS case. In other words, the estimation based on (33)−(36) is quite excellent. It also indicates that the assumptions we made in (33) are reasonable. Therefore, given a profile of buoyancy factor, now we can first calculate the corresponding $B_{\rm av}$, $B_{\rm sd}$, and $B_{\rm sk}$, and then use (33)−(37) to estimate the critical Rayleigh numbers for both the RR and the SS cases.

4.8 Effect of a Buoyancy Factor Profile with a Sign Change

So far we have examined many variable buoyancy factor profiles, but none of them changes sign in the flow domain. For all those buoyancy factor profiles, none of the corresponding $\tilde{u}_3$ eigenfunctions has interior zero points (see Figures 3, 5, 9−10, 14−17, and 19), which implies that it is impossible to have a multiple–layer structure in the field. However, Hsui and Riahi (2000) pointed out that for nearly insulating and rigid boundaries, if the buoyancy factor changes sign in the field, the $\tilde{u}_3$ eigenfunction may have interior zero points, which suggests that multiple–layer flow structure may be possible. Therefore, it is of interest to examine some buoyancy factor profiles that have a sign change in the domain $-1 \leq z \leq 1$ and see how such profiles affect the linear behavior of the thermal convective system.

Following Hsui and Riahi (2000), a parabolic buoyancy factor profile is chosen for this investigation, i.e.

$$B(z) = 1 - 4\epsilon_2 z + \epsilon_2 z^2 \,,$$

where the reference of the buoyancy factor is chosen such that the buoyancy factor at either the top or the bottom boundary becomes unity, and ϵ_2, as we used in Section 4.5, is the buoyancy factor deficit parameter.

Using the same boundary conditions as prescribed in Section 3, we examined a series of parabolic gravity profiles corresponding to deficit parameter ϵ_2 between 1.0 and 1.45. For each given ϵ_2, we solve the associated eigenvalue problem for $\sigma \in [0.0001, 20.0]$ and $Ra \in [100.0, 250000.0]$ (In this investigation, we are dealing with heavy buoyancy factor deficit, which dramatically increases the critical Rayleigh number, compared with the CB case. That is why we set the upper limit of Ra to be as high as 250000 when computing the neutral curves. In fact, when $\epsilon_2 = 1.45$, the corresponding critical Rayleigh number is as high as 241979.) to obtain the neutral curve that yields results of the critical Rayleigh number and the corresponding critical wavenumber of the perturbation.

The results of the critical Rayleigh number and the critical wavenumber are shown in Figure 20. It is noticed that there is a sudden change of slope for both the $(\mathrm{Ra})_{\mathrm{cr}}$vs.$\epsilon_2$ curve and the σ_{cr}vs.ϵ_2 curve, around $\epsilon_2 = 1.168$. In fact, after examining the shape of the $\tilde{u}_3$ eigenfunction, we found that the change of slope corresponds to the change from a single–layer structure to a multiple–layer structure. Another interesting thing is, in previous subsections we found that the critical wavenumber does not depend on the buoyancy factor profiles, as long as there is no sign change of the buoyancy factor within the flow field. This time, however, the critical wavenumber increases as the buoyancy factor deficit parameter ϵ_2 increases.

Seven different shapes of the $\tilde{u}_3$ eigenfunction are found in this investigation as ϵ_2 increases up to 1.45 (Figure 21). Type I has only one local maximum, no local

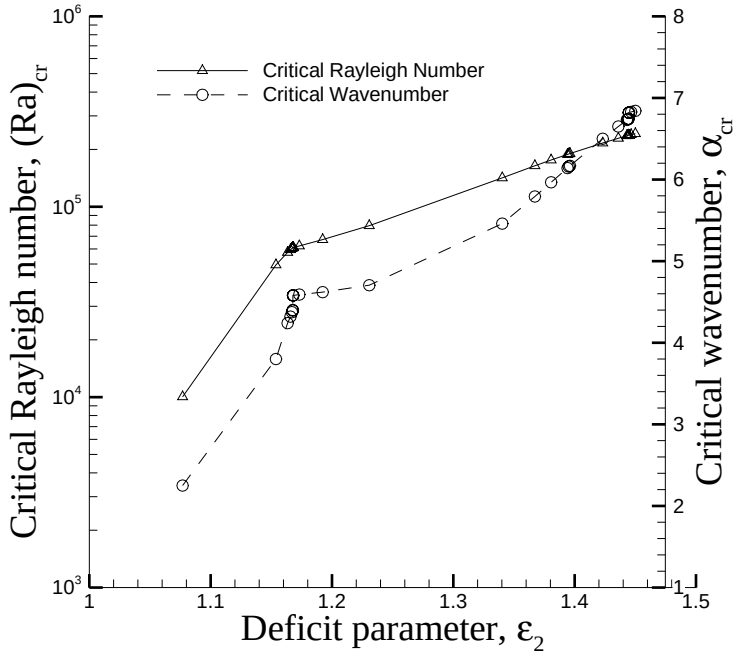

Figure 20. The effect of buoyancy factor deficit parameter on the critical conditions.

minimum, and no internal zero point. The $\tilde{u}_3$ eigenfunction of type I is symmetric with respect to the centerline $z = 0.5$. Type II has two local maximum points, which have the same positive maximum value, one local minimum point which has a positive minimum value, and no internal zero point. The shape of type II is also symmetric with respect to the centerline. Type III has one local maximum point, which has a positive maximum value, one local minimum point, which has a negative minimum value, and one internal zero point at $z = 0.5$. The shape of type III is antisymmetric with respect to the centerline, and there is a zone (about $0.35 \leq z \leq 0.65$) where the $\tilde{u}_3$ eigenfunction is linearly proportional to the depth z. Type IV has almost the same features as type III, except that the linearly proportional zone for type IV (about $0.45 \leq z \leq 0.55$) is much narrower than that for type III. Type V has two local maximum points, which have positive maximum values, and two local minimum points, which have negative minimum values. These local extrema are alternately located, resulting in three internal zero points. It is observed that $z = 0.5$ is always a zero point, and the other two zero points are located symmetrically with respect to the centerline. The shape of type V is antisymmetric with respect to the centerline. Type VI has almost the same features as type V, except that the shape is no longer antisymmetric. Type VII has two local maximum points, which have the same positive maximum value, one local minimum point, which has negative minimum value, and two internal zero points.

The shape of type VII is symmetric with respect to the centerline.

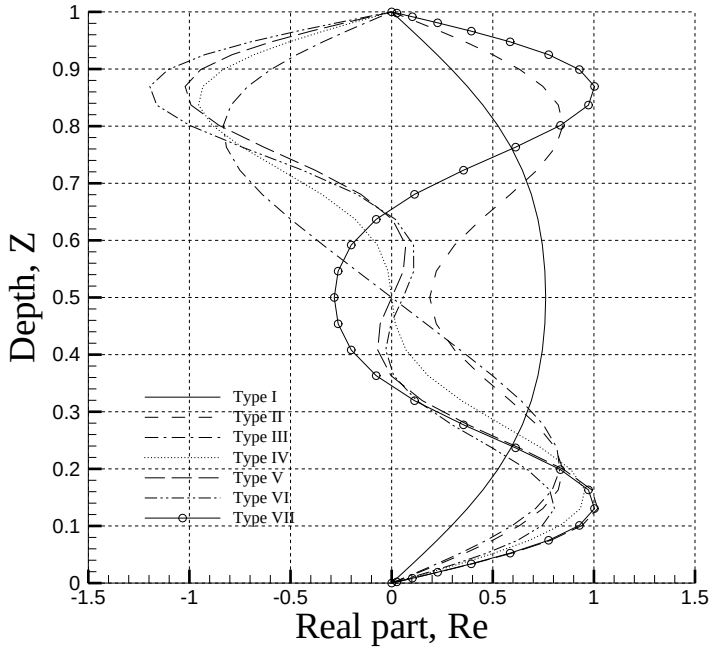

Figure 21. The seven shapes of the $\tilde{u}_3$ eigenfunction.

It is interesting to see how the $\tilde{u}_3$ eigenfunction changes its shape as ϵ_2 increases. Results in Section 4.5 show that, for ϵ_2 less than 1, the $\tilde{u}_3$ eigenfunction is always type I. As ϵ_2 increases to a certain number between 1.0769 and 1.1538, the $\tilde{u}_3$ eigenfunction starts to deform at the middle. (Our main purpose of this investigation is to see whether or not the multiple–layer structure is possible for buoyancy factor profiles with a sign change in the field. Since the change from type I to type II does not mean the appearance of the multiple–layer structure, it is beyond our interest to determine the value of the certain number we mentioned here.) As a result, $z = 0.5$ is no longer the local maximum point. Instead, it becomes the local minimum point, and two local maximum points appear symmetrically beside it. As ϵ_2 increases further, the minimum value keeps decreasing and the maximum value keeps increasing. When ϵ_2 increases from 1.1677 to 1.1678, all of sudden the shape of the $\tilde{u}_3$ eigenfunction switches from type II to type III, and the multiple–layer structure appears. Therefore, the critical buoyancy factor deficit parameter in our case is between 1.1677 and 1.1678. The $\tilde{u}_3$ eigenfunction almost keeps the same features as ϵ_2 increases from 1.1678 to a value between 1.2307 and 1.3403. When ϵ_2 exceeds that value, some deformation occurs around the centerline. This is actually the occurrence of type IV. As ϵ_2 keeps increasing, eventually a narrow zone where the $\tilde{u}_3$ eigenfunction is constant forms

around the centerline and a further increase in ϵ_2 brings the type V profile. This occurs when ϵ_2 reaches a certain number between 1.3806 and 1.3941. After that, the two internal zero points other than $z = 0.5$ move away from the centerline, both local maxima increase, and both local minima decrease as ϵ_2 increases. When ϵ_2 exceeds a value between 1.4438 and 1.4443, the $\tilde{u}_3$ eigenfunction is no longer antisymmetric, and it becomes type VI. According to our results, type VI can exist only for a rather narrow range of ϵ_2 ($1.4438 < \epsilon_2 < 1.4445$). For ϵ_2 in this range, an increase of ϵ_2 makes both the maximum and the minimum decrease, and therefore the non-symmetry increase. When ϵ_2 increases from 1.4444 to 1.4445, all of sudden the shape switches from type VI to type VII, and it is symmetric again.

In the linear stability analysis, the existence of internal zero points of the $\tilde{u}_3$ eigenfunction implies the existence of a multiple–layer structure, and the number of the internal zero points plus 1 gives the number of vertical layers in the flow. Therefore, according to the above results, we say that type I and II correspond to a single–layer structure, type III and IV correspond to a double–layer structure, type VII corresponds to a triple–layer structure, and type V and VI correspond to a quadri–layer structure.

5 Fully Nonlinear Simulation and Results

5.1 Governing Equations

For a fully nonlinear simulation, we start with the governing equations (17)−(19). As in the linear stability analysis, the important parameters are the Rayleigh number Ra, the Prandtl number Pr, the dissipation number Di, and the internal heating parameter H. For our case studies, we assume $\mathrm{Di} = 0$ and $\mathrm{Pr} \to \infty$, so that the nonlinear inertia terms in (18) drop out, and the only nonlinearities retained are the nonlinear convection terms in the energy equation.

In this paper, periodic conditions are chosen in the horizontal directions. As to the vertical boundary conditions, we chose stress–free conditions for the horizontal velocity components, a no–penetration condition for the vertical velocity, and an isothermal condition for the temperature. Thus, the boundary conditions considered here are (21b), (22) and (23a).

5.2 Numerical Method

For the nonlinear simulation, we follow a spectral Fourier–Chebyshev collocation method developed by Balachandar and Yuen (1994). The spectral method is chosen for its exponential convergence and its superior resolution of a wide range of length scales associated with the complex flows. A Chebyshev expansion is used in the vertical

direction to take care of the non–periodic behavior in that direction, while the periodic horizontal boundary conditions are implemented with a Fourier expansion in these directions.

The numerical procedure can be outlined in the following four steps (Balachandar and Yuen, 1994):

(i) Temperature step:
Temperature equation in Fourier space is solved by using an explicit three–stage Runge–Kutta scheme for the nonlinear terms and an implicit Crank–Nicholson scheme for the linear terms.

(ii) Vertical velocity step:
The vertical velocity and the pressure can be connected by an algebraic relation in the Fourier space, so we can finally obtain a linear algebraic system for the vertical velocity (in the Fourier space) only. The boundary pressures are evaluated through the influence matrix technique (Canuto *et al.*, 1988).

(iii) Pressure step:
Once the vertical velocity is known, the pressure can be solved in the Fourier space by using the algebraic relation mentioned in step (ii).

(iv) Horizontal velocity step:
The reduced matrix technique (Canuto *et al.*, 1988) is employed to eliminate the boundary velocity values from the linear algebraic system.

Our numerical code is derived from the original code of Balachandar and Yuen (1994). Modifications are made to implement variable buoyancy factor profiles and some data processing. All these modifications are interface–type, and the core of the algorithm implementation has been kept unchanged.

5.3 Numerical Results

For the nonlinear simulation, we have tested six different profiles of buoyancy factor. The first three are buoyancy factor profiles that have no sign change within the flow domain, and the second three are profiles that have a sign change in the domain. For each case, we had two choices to start the simulation. One is to start from a motionless state with a linear temperature profile. The other is to start from a given flow field previously calculated. For the former choice, we usually introduced a small artificial sinusoidal temperature perturbation so that the development of a flow can be induced. The wavelength of the disturbance is chosen such that the disturbance is linearly unstable.

5.3.1 Numerical Results for Buoyancy Factor Profiles Without Sign Change

For this investigation, we have tested three buoyancy factor profiles: a constant profile (i.e. a CB case that has a critical Rayleigh number of about 657), an $\epsilon_2 = 0.25$ parabolic profile (i.e. a 25% para–VB case that has a critical Rayleigh number of about 840), and an $\epsilon_2 = 0.50$ parabolic profile (i.e. a 50% para–VB case that has a critical Rayleigh number of about 1200). Results of the simulation for Ra = 5000 are shown in Figures 22 and 23. For this calculation, the CB case is started with a motionless state with a linear temperature profile, while the simulations for both the 25% para–VB and the 50% para–VB cases are started with the flow field corresponding to the CB case after 21500 timesteps. As a result, the simulation for the CB case takes more than 10000 time steps (about 33 CPU hours on the NCSA's Origin–2000 machine) for the flow field to reach a steady state, while it takes only about 5500 timesteps (about 18 CPU hours) for both the 25% para–VB and the 50% para–VB cases to reach a steady state (Figure 22).

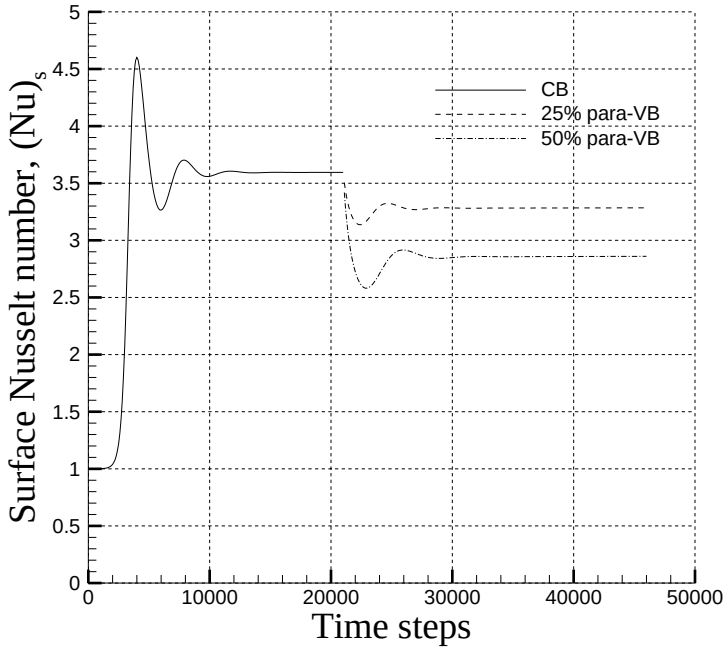

Figure 22. Evolution of the surface Nusselt number for Ra=5000.

Figure 22 presents the surface Nusselt number $(Nu)_s$ as a function of numerical time steps. It illustrates the evolution of the dynamic flow. For the three buoyancy factor profiles that we have investigated, the surface Nusselt numbers tend to settle at about 3.597, 3.287, and 2.864, respectively. These results indicate that a deficit in buoyancy factor reduces the surface Nusselt number significantly (every 25% buoyancy

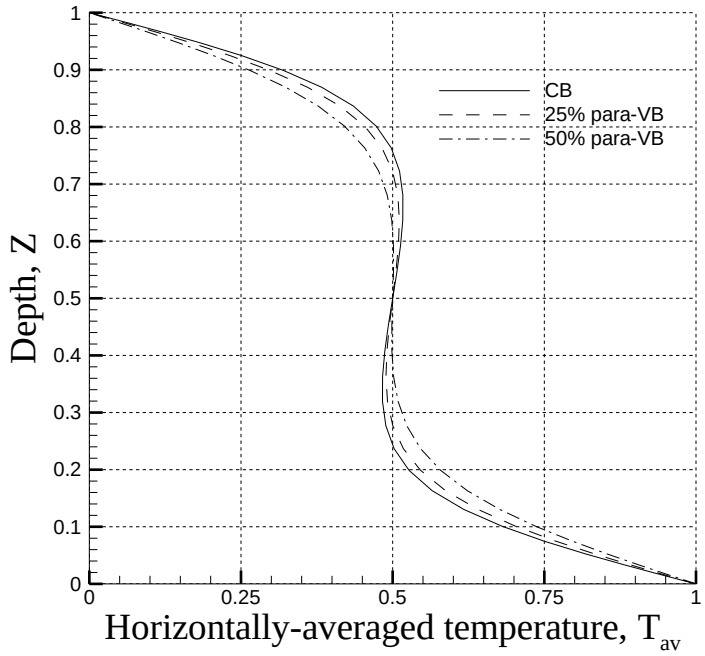

Figure 23. Horizontally–averaged temperature profile for Ra=5000.

factor deficit causes about 10% reduction in the surface Nusselt number).

Figure 23 shows the steady–state horizontally–averaged temperature profiles across the fluid layer for these three cases. We checked the relative difference of temperature at every gridpoint in our computational domain and found that the averaged relative temperature difference is about 6% between the CB case and the 25% para–VB case, and about 12% between the CB case and the 50% para–VB case.

In our simulation, we also examined the flow structure. For this Rayleigh number, a two–dimensional roll structure along the x direction is observed. All the three cases show a structure qualitatively similar to the ones shown in Figures 24 and 25, where Figure 24 is a velocity vector plot of the flow cells, and Figure 25 represents the corresponding isothermal structure.

The simulation for these three buoyancy factor profiles has also been carried out for Ra = 10000. At this Rayleigh number, the surface Nusselt numbers are found to be 4.681, 4.362, and 3.948, respectively, for the CB case, the 25% para–VB case and the 50% para–VB case. The corresponding averaged relative temperature difference is about 13% between the CB case and the 25% para–VB case, and about 17% between the CB case and the 50% para–VB case. Compared with the results of Ra = 5000, the surface Nusselt number drops a bit faster as the buoyancy factor deficit increases (Figure 26), and the averaged relative temperature difference between the CB case and

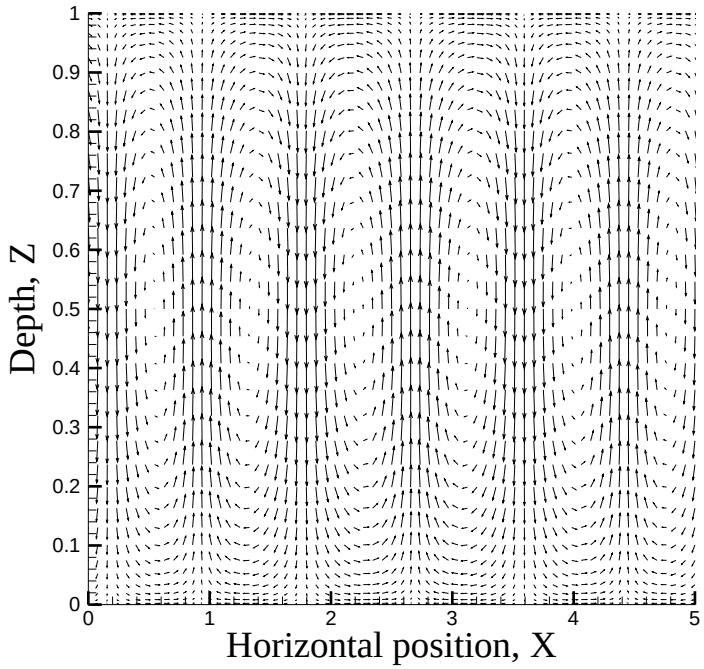

Figure 24. Velocity vector plot for Ra=5000.

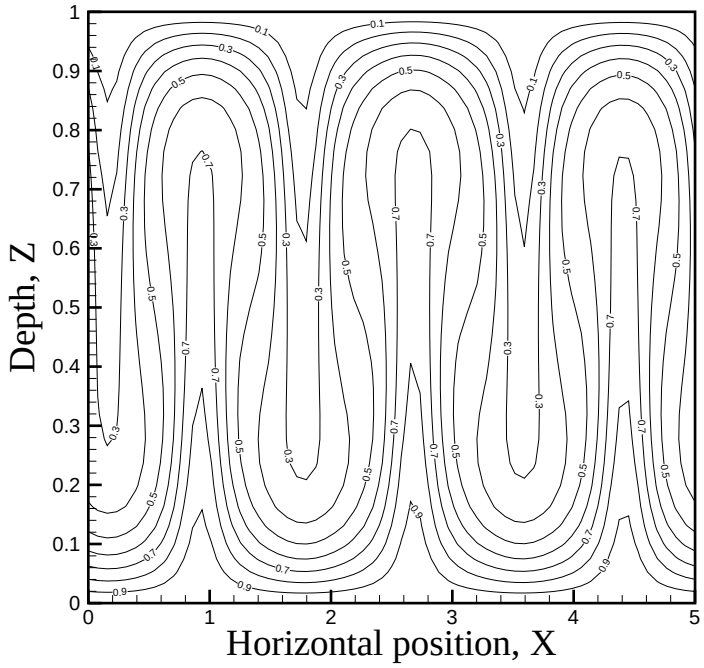

Figure 25. Temperature isosurface plot for Ra=5000.

the VB cases becomes larger. The flow structure, on the other hand, remains the same as two–dimensional rolls.

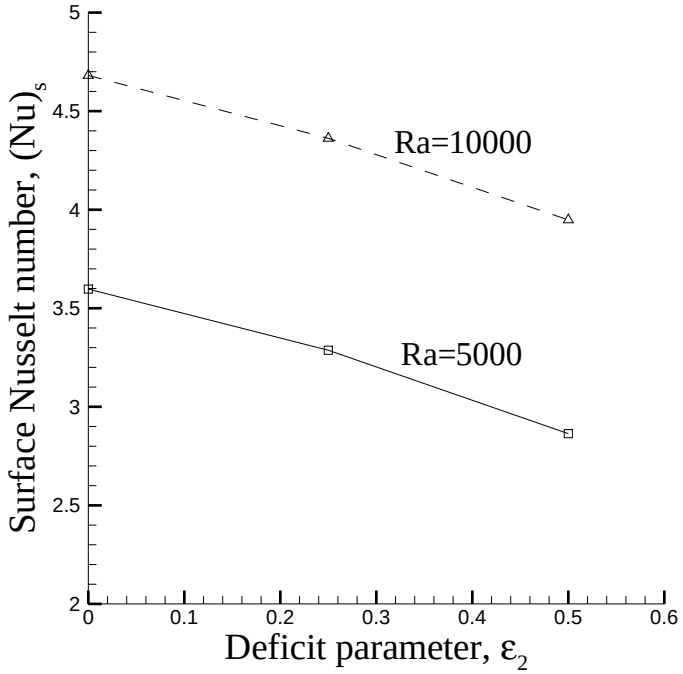

Figure 26. The effect of buoyancy factor deficit on the surface Nusselt number.

5.3.2 Numerical Results for Buoyancy Factor Profiles With a Sign Change

For this investigation, we chose three parabolic buoyancy factor profiles to study: ϵ_2 =1.10, 1.25, and 1.45, respectively. According to the linear stability results in Section 4.9, these three profiles correspond to a single–layer structure, a double–layer structure, and a triple–layer structure, respectively. The conditions used in these simulations are listed in Table IX, where $(\mathrm{Ra})_{\mathrm{cr}}$ and σ_{cr} are the critical conditions predicted by the linear stability analysis (Figure 20), Ra is the selected Rayleigh number for this investigation, σ is the wavelength of the initial artificial disturbance, and ω is the nondimensional temporal growth of the initial disturbance predicted by the linear stability analysis.

The flow structures we obtained in these three cases are shown in Figures 27−32. From the velocity vector plots (Figures 27, 29, and 31), we see that a single–layer structure exists when $\epsilon_2 = 1.10$ (Figure 27), a double–layer structure exists when $\epsilon_2 = 1.25$ (Figure 29), and a triple–layer structure exists when $\epsilon_2 = 1.45$ (Figure 31). In fact, in the $\epsilon_2 = 1.25$ case, the vertical velocity equals zero at $z = 0.5$, and thus $z = 0.5$ is the dividing line between the two layers. In the $\epsilon_2 = 1.45$ case, comparatively,

Case	ϵ_2	$(\mathrm{Ra})_{\mathrm{cr}}$	σ_{cr}	Ra	σ	ω
Case110	1.10	21886.2	2.716	40000	2.80	10.61
Case125	1.25	90465.3	4.838	100000	4.40	3.61
Case145	1.45	241979.0	6.841	300000	7.00	13.60

Table IX. The conditions used in the nonlinear simulations for $\epsilon_2 > 1.0$

there are two dividing lines, located at about $z = 0.36$ and $z = 0.64$, respectively. The corresponding temperature isosurfaces (Figures 28, 30, and 32) also show quite different features. In the $\epsilon_2 = 1.10$ case, a temperature isosurface can have a rather large penetration depth (Figure 28). In the $\epsilon_2 = 1.25$ case, isosurfaces for $T > 0.5$ are confined in the lower half of the domain, whereas isosurfaces for $T < 0.5$ are confined in the upper half, and the $T = 0.5$ isosurface is located right at the middle ($z = 0.5$) (Figure 30). In the $\epsilon_2 = 1.45$ case, isosurfaces for $T \geq 0.7$ are confined in the sub-domain $z < 0.35$, and isosurfaces for $T \leq 0.3$ are confined in the sub-domain $z > 0.65$. In the remaining region ($0.35 \leq z \leq 0.65$), all the temperature isosurfaces are almost flat lines, showing that in that region the velocity is very small and the thermal structure is very close to a conductive layer (Figure 32).

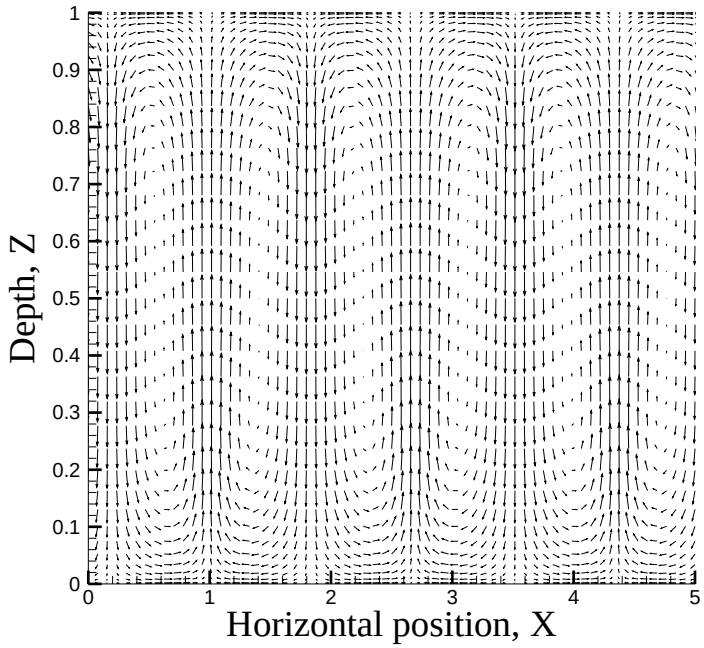

Figure 27. Velocity vector plot in $\epsilon_2 = 1.10$ case.

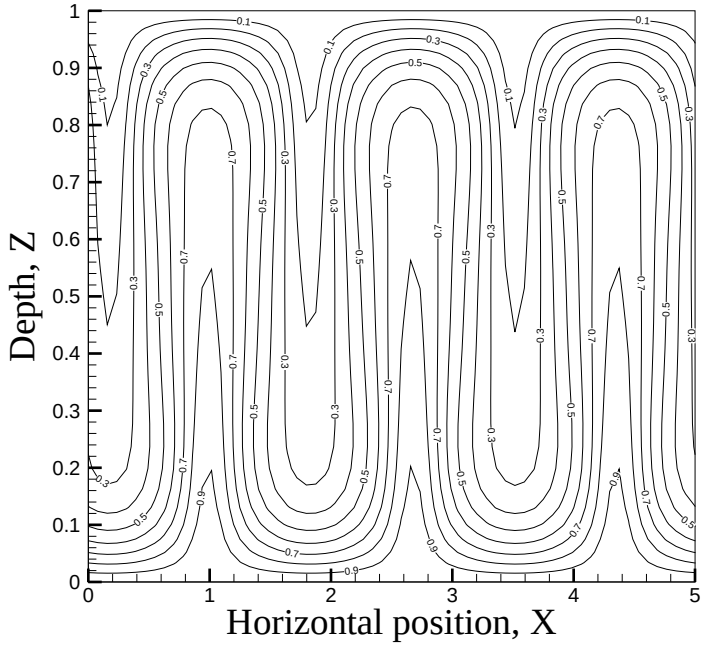

Figure 28. Temperature isosurface in $\epsilon_2 = 1.10$ case.

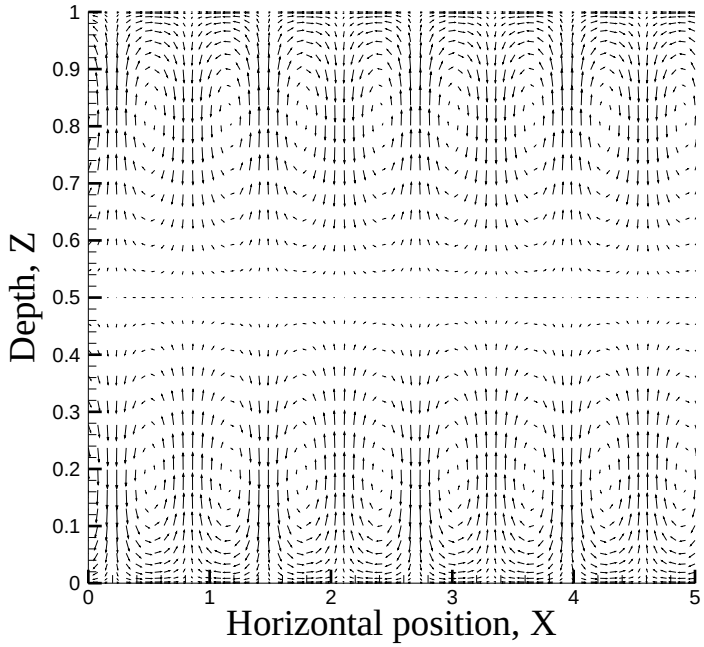

Figure 29. Velocity vector plot in $\epsilon_2 = 1.25$ case.

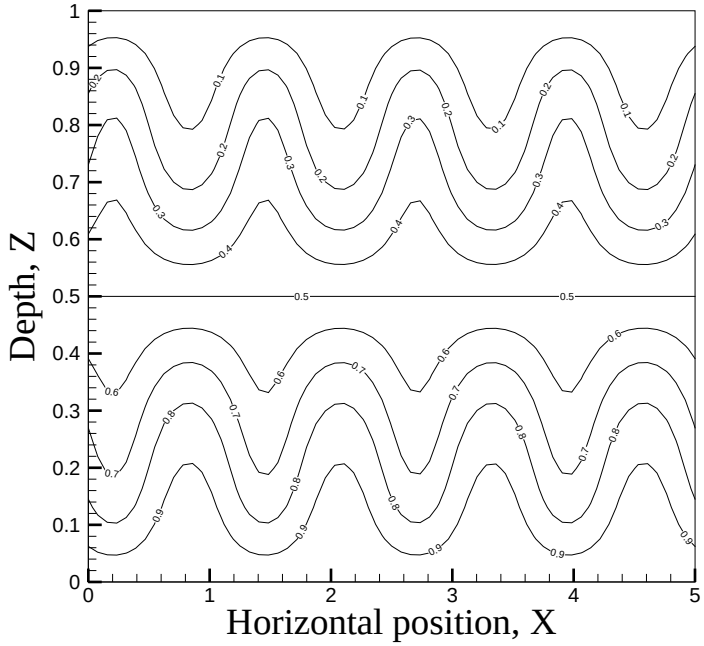

Figure 30. Temperature isosurface in $\epsilon_2 = 1.25$ case.

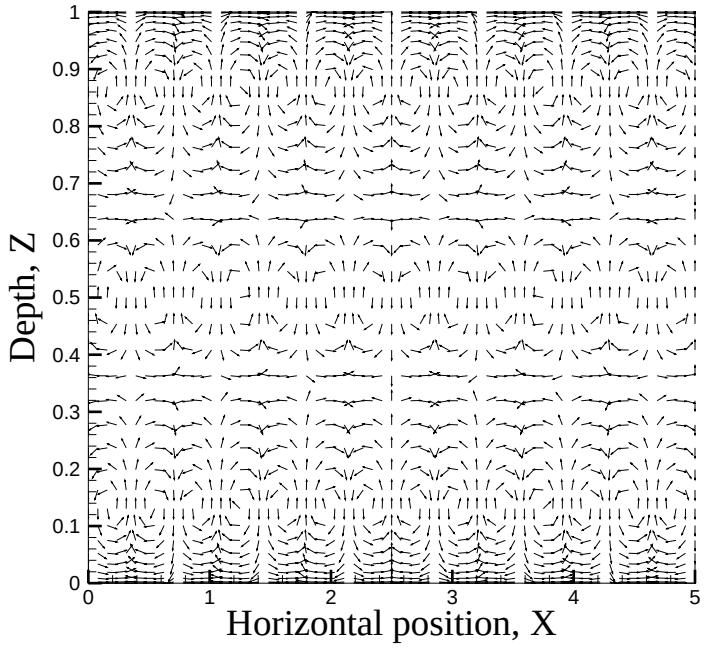

Figure 31. Velocity vector plot in $\epsilon_2 = 1.45$ case.

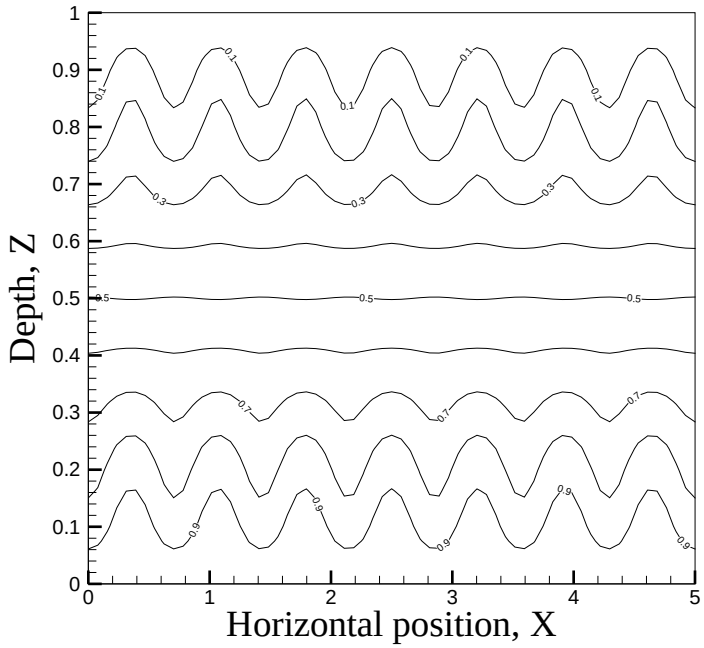

Figure 32. Temperature isosurface in $\epsilon_2 = 1.45$ case.

The surface Nusselt number $(\mathrm{Nu})_s$ in these three cases are 4.081, 1.237, and 1.102, respectively. These results indicate that when the buoyancy factor deficit becomes very heavy, the surface Nusselt number decreases very rapidly, and finally it does not differ significantly from 1.0, the surface Nusselt number for a conductive layer. The profiles of the horizontally averaged temperature in these three cases are shown in Figure 33. In the $\epsilon_2 = 1.10$ case, a large difference from the linear horizontally-averaged temperature profile can be observed. In the $\epsilon_2 = 1.25$ and $\epsilon_2 = 1.45$ cases, on the other hand, the difference from the linear temperature profile is not very large. This result is consistent with the result for the surface Nusselt number.

6 Conclusions and Remarks

In this paper, we have carried out the linear stability analyses and fully nonlinear simulations to investigate thermal convection between two infinite horizontal planes with different vertically varying buoyancy factors. An isothermal boundary condition is used for both boundaries. By solving the linear stability eigenvalue problem numerically, we reach the following conclusions:

(i) Buoyancy factor deficits yield higher critical Rayleigh numbers than that in the CB case. The more the deficit is, the higher the critical Rayleigh number becomes.

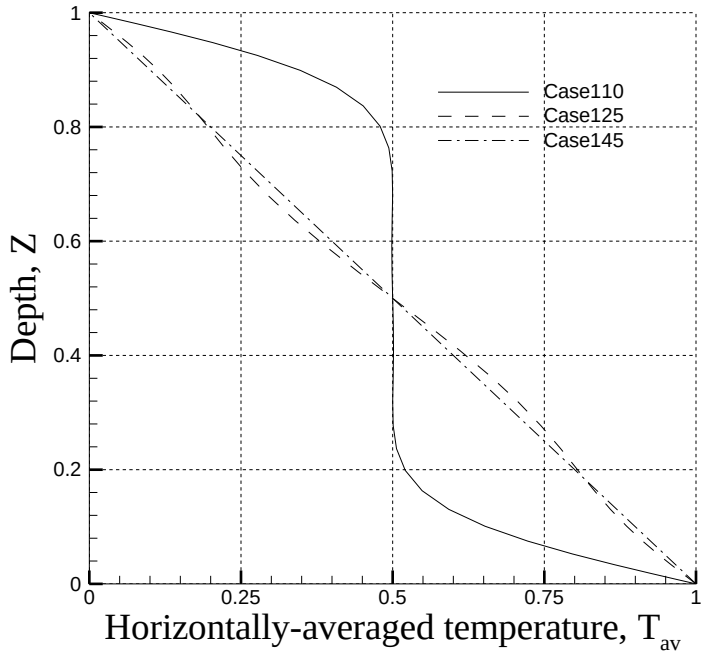

Figure 33. Horizontally–averaged temperature profiles in nonlinear simulations.

(ii) When the buoyancy factor does not change sign throughout the field, the critical wavenumber is independent of the buoyancy factor profiles. When there is a sign change of the buoyancy factor in the field, however, the critical wavenumber increases with the buoyancy factor deficit.

(iii) With regard to the $\tilde{u}_3$ eigenfunction, buoyancy factor variations have only very small effects on the shape of the eigenfunction, provided there is no sign change in the buoyancy factor. If there is a sign change, the shape of the $\tilde{u}_3$ eigenfunction can change significantly as the buoyancy factor changes. In fact, for parabolic profiles with a sign change, seven different shapes of the $\tilde{u}_3$ eigenfunction have been observed in this investigation.

(iv) When the buoyancy factor does not change sign throughout the fluid layer, the effects of the buoyancy factor variation on the critical Rayleigh number can be approximated by a function of up to the third–order moment of the variable buoyancy factor profile, and this approximation gives quite a good estimate of the critical Rayleigh number.

(v) A critical value close to 1.1677 has been found for the buoyancy factor deficit parameter ϵ_2. When ϵ_2 is less than the critical value, there is no interior zero point for the $\tilde{u}_3$ eigenfunction, and thus only a single–layer structure is possible.

When ϵ_2 is greater than the critical value, on the other hand, there exist interior zero point(s) for the $\tilde{u}_3$ eigenfunction, and therefore multiple–layer structures may be possible.

The results of our fully nonlinear computational study for parabolic profiles of buoyancy factor with no sign change, at Ra = 5000 and 10000, and for Pr $\to \infty$, yield the following conclusions:

(i) The surface Nusselt number decreases with increasing deficit parameter ϵ_2. The rate of change of the heat flux with respect to ϵ_2 is about 10% for every 25% parabolic buoyancy factor deficit.

(ii) The horizontally–averaged temperature has about 10% difference between the CB case and the VB cases. The larger the buoyancy factor deficit is, the larger the relative difference is. Also, the larger the Rayleigh number is, the larger the relative difference is.

(iii) The flow structure, however, is qualitatively the same for all the three buoyancy factor profiles that we have tested. No multiple–layer structure in the vertical direction is detected.

Nonlinear simulations for three parabolic buoyancy factor profiles with a sign change in the field have also been carried out, for Rayleigh numbers not quite above the corresponding critical Rayleigh numbers (Table IX). The following conclusions can be drawn from this investigation:

(i) The one with the least buoyancy factor deficit shows a single–layer structure, while the other two yield multiple–layer structures. These results agree with the predictions of the linear stability analysis.

(ii) As the buoyancy factor deficit increases, the flow field breaks into multiple layers, and the depth of each layer becomes smaller. As a result of the structure change, the convection efficiency of the system decreases, resulting in a lower surface Nusselt number.

In this study, we have carried out investigations only for fluid layers with isothermal boundary conditions. However, our model can also be extended to incorporate other types of thermal boundary condition.

With regard to the horizontal flow structure for the present convection problem, it is expected (Riahi, 1996) that two–dimensional rolls, detected in the present study, should govern over an extensive range of the supercritical domain (Ra $>$ $(\mathrm{Ra})_{\mathrm{cr}}$), except for very small amplitude of subcritical convection for an asymmetric buoyancy factor

profile with respect to the mid-plane of the layer, where hexagonal cells can be realized in a small subcritical domain. However, for the far–supercritical domain ($\mathrm{Ra} \gg (\mathrm{Ra})_{\mathrm{cr}}$), a three–dimensional structure will dominate. To reach a more realistic simulation of the dynamical behavior within planetary interiors, nonlinear stability analysis and fully nonlinear numerical simulation using more specific physical parameters and at large Ra ($\mathrm{Ra} \gg (\mathrm{Ra})_{\mathrm{cr}}$) are necessary.

Finally, it should be noted that in our present nonlinear simulations for the multiple–layer structure, the selected Rayleigh numbers are not far above the critical values. It would be of interest to study the behavior of the convective system under Rayleigh numbers that are far above the critical ones. Such studies would be able to address if a multiple–layer structure can be maintained under large supercritical Rayleigh numbers.

Acknowledgments

This research was supported by the UIUC Research Board, the National Center for Supercomputing Applications (NCSA) under grant EAR000001N, and the National Partnership for Advanced Computational Infrastructure (NPACI). The computer code for the numerical simulations was generously made available by Prof. S. Balachandar.

References

Anderson, D. L., and Hart, R. S., "An Earth model based on free oscillations and body waves", *J. Geophys. Res.* **81**, No. 8, 1461–1475 (1976).

Balachandar, S., and Yuen, D. A., "Three–dimensional fully spectral numerical method for mantle convection with depth–dependent properties", *Journal of Computational Physics* **113**, 62–74 (1994).

Canuto, C., Hussaini, M. Y., Quarteroni, A., and Zang, T. A., "Spectral methods in fluid dynamics", Springer–Verlag, New York (1988).

Chandrasekhar, S., "Hydrodynamic and hydromagnetic stability", Oxford, Clarendon Press (1961).

Hsui, A. T., and Riahi, D. N., "Some remarks about buoyancy and mantle convection within planetary interiors", submitted to *J. Geodynamics* (2000).

Jarvis, G. T., and McKenzie, D. P., "Convection in a compressible fluid with infinite Prandtl number," *J. Fluid Mech.* **96**, 515–583 (1980).

Press, W. H., Teukolsky, S. A., Vetterling W. T., and Flannery, B. P., "Numerical recipes in Fortran 77, The Art of Scientific Computing" (2nd ed.), Cambridge University Press, 487–489 (1996)

Riahi, D. N., "Nonlinear stability analysis and modeling for convective flows", in *Mathematical Modeling and Simulation in Hydrodynamic Stability* (ed. D. N. Riahi), World Scientific Publishing Co., 117–148 (1996).

Schubert, G., "Introduction to dynamics of the solid Earth and other planets", *Rev. of Geophys.*, Supplement to Vol. **13**, 195–197 (1995).

Stacey, F. D., "Physics of the Earth" (3rd edition), Appendix F, Brookfield Press, Brisbane, Australia 454–455 (1992).

Turcotte, D. L., Torrance K. E., and Hsui A. T., "Convection in the Earth's mantle" in *Methods in Computational Physics, Advances in Research and Applications*, Vol. **13**, Academic Press, New York 431–454 (1973).

White, F. M. , "Viscous fluid flow", second edition, McGraw-Hill Inc., New York (1991).